In Search of the Standard Model Higgs Boson

by

Ross I. Berbeco

A dissertation submitted in partial fullfilment
of the requirements for the degree of
Doctor of Philosophy
(Physics)
in The University of Michigan
2002

Doctoral Committee:

Professor J. Keith Riles, Chair
Professor Tim McKay
Professor Byron P. Roe
Professor Lawrence Sklar
Professor York-Peng Yao

ABSTRACT

In Search of the Standard Model Higgs Boson

by

Ross I. Berbeco

Chair: Professor J. Keith Riles

A search for the Standard Model Higgs boson is conducted using data from the L3 detector at CERN's LEP collider during the year 2000. The integrated luminosity collected was 217.4 pb^{-1} of electron-positron collisions at center-of-mass energies from 200 to 209 GeV. Presented here is a search for $e^+e^- \to hZ$, where the Higgs decays into b quarks and the Z boson decays into undetected neutrinos. Also presented are combined results from the other L3 channels. The L3 combined results are consistent with the Standard Model background. Preliminary results from the LEP-wide combination are also shown. The lower limit on the Standard Model Higgs mass is found to be

$$m_h > 114.1 \text{ GeV at } 95\% \text{ C.L.}$$

In the LEP combination, an excess of data events is observed near $m_h \sim 115.6$ GeV. Whether this is due to a statistical fluctuation or to Higgs production cannot be determined from the available set of data.

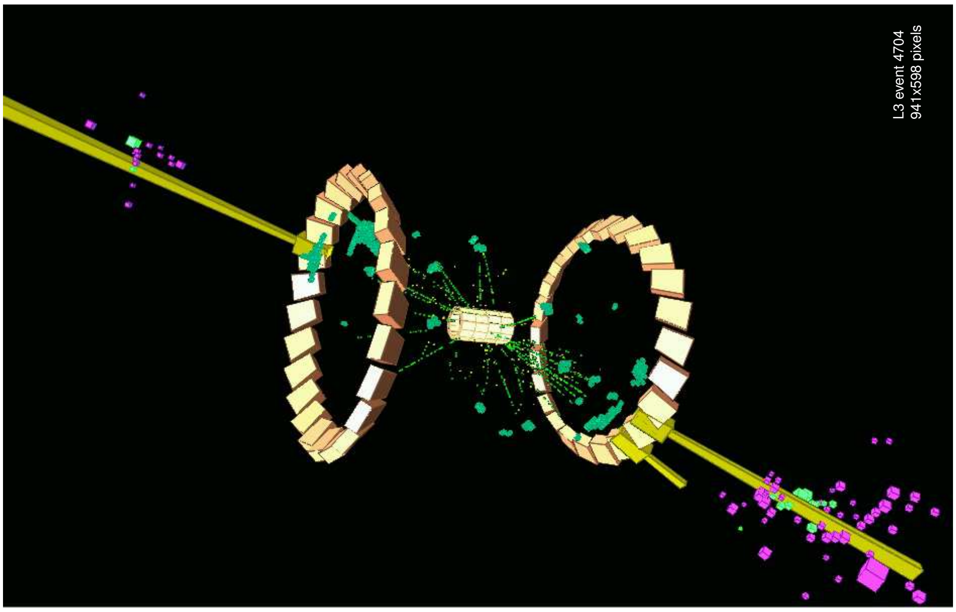

“The decision was agonizing. For weeks, petitions circulated, rumors flew, minds changed overnight; evidence that looked solid Wednesday evaporated by Thursday. And then it was over.”

-K.C. Cole, LA Times, Dec. 5, 2000, Column One.

ACKNOWLEDGMENTS

The work presented here would not have been possible without the help of many people. I would like to take this opportunity to thank them.

While working on the Higgs search, I felt as though I had two advisors. At Michigan, I benefitted from the wisdom and teachings of Keith Riles. He gave more time than he had and it was all greatly appreciated. I wish to someday have his sagacity and physics ability. At CERN, I received limitless support from the indefatigable Chris Tully. In addition to his sound advice and unbridled enthusiasm, he also shared his friendship, his office and his apartment. From him, I learned first hand what it takes to be a great physicist. Also aiding me at CERN were J.J. Blaising, Marta Felcini, Pablo Garcia-Abia, Andre Holzner and Andrei Kunin. I wish to also acknowledge the entire L3 collaboration and its spokesman, Samuel C.C. Ting, for having faith in my work. From Michigan, I learned a great deal from conversations with Byron Roe and Larry Jones. Their depth of knowledge and willingness to share it was well received.

A special thanks is due to Jin Yamamoto, who with friendship, good cheer and late night gifts of food, kept me sane and productive during a very difficult time. I honestly don't know if I could have done it without him. Also, deserving of sincere appreciation, is Brooke Scelza whose presence made the burden bearable and the journey a delight.

Last, but certainly not least, my family should be recognized for their unflagging encouragement and love.

INTRODUCTION

The Higgs boson is crucial to our understanding of the fundamental nature of the universe. Although it plays an important role in the theoretical model of particle interactions, there is no direct experimental evidence of its existence. Discovery of the Higgs boson would put an important issue in particle physics to rest, confirming at least part of the prevailing model of particle mass generation. Exclusion of its existence, however, would be an important result too as it would indicate a serious flaw in the theory.

Searches for the Higgs Boson have been conducted for many years at several different particle accelerators, all with negative results. Therefore, as the energies of the machines increase, so does the lower mass limit. The work presented here represents the final results of the LEP collider. There will be a brief introduction to the theory behind the Higgs mechanism including expected production and decay properties, a description of the experimental apparatus and a more in-depth look into the analysis and the results.

The search for the Higgs is one of the most exciting frontiers in experimental particle physics. Hundreds of physicists, internationally, are involved in this endeavor. Several future accelerators among whose goals is to discover or study the Higgs boson are in various stages of planning, construction or commissioning. Although the LEP results are negative, it is possible that we may have seen the first indication of the Higgs boson, which adds a feeling of expectancy to an already thrilling pursuit.

CONTENTS

CHAPTER

LIST OF FIGURES

Figure

LIST OF TABLES

Table

LIST OF APPENDICES

Appendix

CHAPTER 1

Theory

1.1 The Standard Model

The Universe is believed to be composed of a set of fundamental sub-atomic particles whose properties are predicted by a theory called the Standard Model [1]. This theory divides up these basic building blocks into two categories: fermions and bosons. The fermions have spin 1/2 and are the constituents of all matter. Bosons have integer spin and act as go-betweens for the fermions, mediating all interactions between them. Fermions can be further divided into two groups of particles, leptons and quarks. Both of these groups come in three "generations" with each generation containing two particles. Additionally, every fermion has an anti-particle associated with it that has equal mass but oppositely signed quantum numbers. So, in total, there are 24 fermions. The leptons include electrons, muons, taus and each of their respective neutrinos:

$$\begin{pmatrix} e \\ \nu_e \end{pmatrix} \begin{pmatrix} \mu \\ \nu_\mu \end{pmatrix} \begin{pmatrix} \tau \\ \nu_\tau \end{pmatrix} \tag{1.1}$$

The quarks are (in order of lightest to heaviest) up, down, strange, charm, bottom and top.

$$\begin{pmatrix} u \\ d \end{pmatrix} \begin{pmatrix} c \\ s \end{pmatrix} \begin{pmatrix} t \\ b \end{pmatrix} \tag{1.2}$$

Every one of these fermions has been observed by experiments. Their properties are listed in a table below.

	quarks			leptons	
symbol	mass (GeV)	charge	symbol	mass (MeV)	charge
u	(1-5) × 10^{-3}	2/3	e	0.511	-1
d	(3-9) × 10^{-3}	-1/3	ν_e	$< 3.0 \times 10^{-3}$	0
c	1.15-1.35	2/3	μ	105.7	-1
s	(75-170) × 10^{-3}	-1/3	ν_μ	< 0.19	0
b	4-4.4	2/3	τ	1777	-1
t	174.3 ± 5.1	-1/3	ν_τ	< 18.2	0

Table 1.1. The fermion masses and electric charges [2].

The other class of particles, the gauge bosons, are the mediators of the four basic forces of nature: electromagnetic, weak, strong and gravity. The photon, which is responsible for electromagnetic interactions, has been known to us in some form for centuries. Our eyes are excellent photon detectors within a narrow band of energies. The weak force is more hidden from us and the gauge bosons associated with it, W and Z can only be "observed" via their decay products in experimental apparatus. Indeed, their existences were confirmed by exactly this method in 1983. Physicists at CERN working at a 540 GeV proton-antiproton collider looked for, and found $p\bar{p} \rightarrow W^{\pm}$X, where the W boson decays semileptonically [3]. The same group also found interactions $p\bar{p} \rightarrow Z^{o}$X where the Z decays to either $e^{+}e^{-}$ or $\mu^{+}\mu^{-}$ [4]. The mediator of the strong force, the gluon, has also not been observed directly, but indirect evidence from particle accelerators is also plentiful. All of the measurements of these bosons as well their interactions with fermions have supported the Standard Model. This theory has been extremely accurate in its depiction of these processes. Gravity, on the other hand, is not at all touched by the Standard Model. The structure of gravity on very small scales is unknown and much theoretical research has been devoted to unifying all of the fundamental forces, including gravity. No experimental evidence, however, has confirmed any unified theory.

Boson	mass	charge	Force mediated
photon(γ)	$< 2 \times 10^{-16}$ eV	0	electromagnetic
$W^{\pm}$	80.42 ± 0.06 GeV	± 1	charged weak
Z	91.188 ± 0.002 GeV	0	neutral weak
gluon	0	0	strong nuclear

Table 1.2. The fundamental forces of nature.

1.2 Gauge invariance

Any theory about the interactions of the fundamental particles should be independent of space-time location. This stipulation leads to the notion of gauge invariance. Given a Lagrangian density ($\mathcal{L}$)[1] we should be able to change the phase at any place and still achieve the same results. This amounts to changing the field ψ by a phase factor that is dependent on x^{μ} (local SU(2) transformation):

$$\psi \rightarrow e^{i\theta}\psi \tag{1.3}$$

where $\theta = \theta(x^{\mu})$. A Lagrangian that undergoes this field transformation and remains unchanged is said to be locally gauge invariant. For the following discussion, it is convenient to define θ as such:

$$\theta(x) \equiv -\frac{q}{\hbar c}\lambda(x). \tag{1.4}$$

When the local gauge transformation is performed on the Dirac Lagrangian,

$$\mathcal{L}_{Dirac} = i\hbar c\bar{\psi}\gamma^{\mu}\partial_{\mu}\psi - mc^{2}\bar{\psi}\psi, \tag{1.5}$$

it is found that $\mathcal{L}_{\mathcal{D}\rangle\nabla\dashv\rfloor}$ is not invariant. Instead, the Lagrangian picks up an extra term from the derivative of λ:

---

[1] From this point on in the text, $\mathcal{L}$ is referred to as the "Lagrangian"

$$\mathcal{L} \rightarrow \mathcal{L} + (q\bar{\psi}\gamma^{\mu}\psi)\partial_{\mu}\lambda. \tag{1.6}$$

A new term should be added to make the Lagrangian locally gauge invariant,

$$(q\bar{\psi}\gamma^{\mu}\psi)A_{\mu}, \tag{1.7}$$

where A_{μ} transforms under local gauge transformations as follows:

$$A_{\mu} \rightarrow A_{\mu} + \partial_{\mu}\lambda. \tag{1.8}$$

The Lagrangian will now be invariant under local gauge transformations. To examine the full Lagrangian, we need to add terms that deal with the self-interaction of the vector field, A_{μ}. For this situation, the Proca Lagrangian is appropriate:

$$\mathcal{L}_{Proca} = -\frac{1}{16\pi}F^{\mu\nu}F_{\mu\nu} + \frac{1}{8\pi}(\frac{m_A c}{\hbar})^2 A^{\nu}A_{\nu}, \tag{1.9}$$

where $F^{\mu\nu} = \partial^{\mu}A^{\nu} - \partial^{\nu}A^{\mu}$ is the electromagnetic field-strength tensor. The first term in the Proca Lagrangian is locally gauge invariant, but the second is not. Therefore, to save local gauge invariance for the complete Lagrangian, we must set m_A equal to zero. Therefore, the complete, locally invariant, Lagrangian for fermions and a vector field is

$$\mathcal{L}_{complete} = i\hbar c\bar{\psi}\gamma^{\mu}\partial_{\mu}\psi - mc^2\bar{\psi}\psi - \frac{1}{16\pi}F^{\mu\nu}F_{\mu\nu} - (q\bar{\psi}\gamma^{\mu}\psi)A_{\mu}. \tag{1.10}$$

Note that by setting $m_A = 0$, we've removed the mass of the gauge field, A_{μ}. This field, however, is really the electromagnetic potential whose associated particles, photons, have been found to be massless. By invoking local gauge invariance, we derived the Lagrangian above which describes the interactions of fermions and photons, i.e. electrodynamics. That the resulting Lagrangian has no mass term for the boson is acceptable for photons and gluons, but not for the W and Z bosons. This wrinkle needs to ironed out in a complete model.

1.3 Spontaneous Symmetry Breaking

1.3.1 Scalar-singlet case

Suppose we begin with the following Lagrangian:

$$\mathcal{L} = T - V = \frac{1}{2}\partial_\mu\phi\partial^\mu\phi - (\frac{1}{2}\mu^2\phi^2 + \frac{1}{4}\lambda^2\phi^4) \tag{1.11}$$

where ϕ is a scalar field and μ and λ are free parameters. Note that there is a symmetry: the equation is invariant under the change $\phi \rightarrow -\phi$. The classic way of examining this potential is to find the vacuum expectation (i.e. require $\frac{\partial V}{\partial \phi} = 0$) and then perturb this minimum slightly to find the excitations. For the given Lagrangian, there are two cases to examine: $\mu^2 > 0$ and $\mu^2 < 0$. In the first case, the minimum of the potential occurs at $\phi = 0$ and the coefficient of the term in second order of the field is the mass. This is comparable to a Klein-Gordon equation. However, there is no *a priori* reason for choosing μ^2 to be positive. Let's look at the case when it is negative. For $\mu^2 < 0$, the minimum of the potential occurs at two places:

$$\phi = \pm\frac{\mu}{\lambda}. \tag{1.12}$$

This is shown in figure 1.1.

So there are two vacuum expectation values ($\phi = \pm\frac{\mu}{\lambda} \equiv v$) at the two minima for this field. By arbitrarily choosing one minimum and then perturbing the field around this point, the particle spectrum of this field can be studied. When we substitute the perturbation $\phi = v + \eta(x)$ into the equation above (1.12), the Lagrangian now looks like this

$$\mathcal{L} = \frac{1}{2}(\partial_\mu\eta\partial^\mu\eta) - (\lambda^2v^2\eta^2 + \lambda^2v\eta^3 + \frac{1}{4}\lambda^2\eta^4) + \frac{1}{4}\lambda^2v^4 \tag{1.13}$$

where the last term is a constant. The term in second order of η is a mass term. So the Lagrangian above describes a particle of mass $m = 2\lambda^2v^2 (= -2\mu^2)$. There

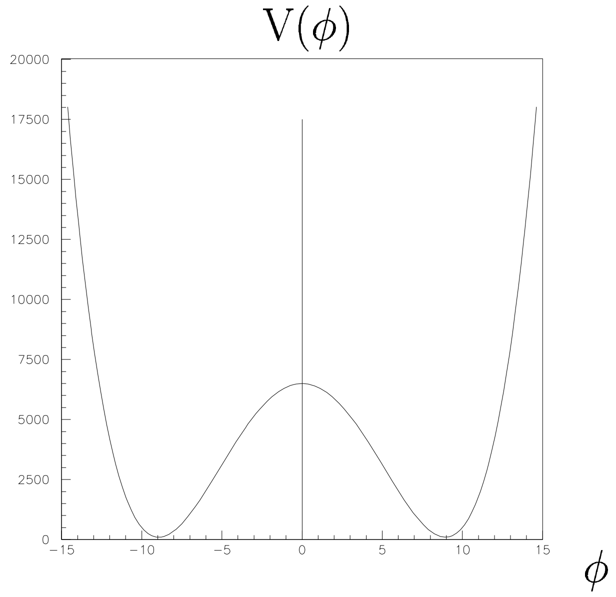

Figure 1.1. The "wine bottle" Higgs potential (after the symmetry is broken). The minimum occurs at two places, $\phi = \pm\mu/\lambda$. The numbers in the figure are arbitrary.

are also cubic and quartic interaction terms of this particle which depend on λ^2 too. It is important to note that λ is a free parameter here so the mass and strength of interactions cannot be predicted. The symmetry $\phi \to -\phi$ is broken in Eq. 1.13 because of the η^3 term in the Lagrangian. This happened because of the arbitrary choice of $\phi = +v$ instead of $\phi = -v$. This phenomenon is called "spontaneous symmetry breaking" because the symmetry is broken by a spontaneous arbitrary choice.

1.3.2 Complex scalar case

The basic example above can be extended from the simple reflection symmetry to a global U(1) symmetry (ex. rotation). To do this, we make the field, ϕ, a complex scalar:

$$\phi = \frac{\phi_1 + i\phi_2}{\sqrt{2}} \tag{1.14}$$

where ϕ_1 and ϕ_2 are real. The Lagrangian then becomes

$$\mathcal{L} = \frac{1}{2}(\partial_\mu\phi_1)^2 + \frac{1}{2}(\partial_\mu\phi_2)^2 - \frac{1}{2}\mu^2(\phi_1^2 + \phi_2^2) - \frac{\lambda}{4}(\phi_1^2 + \phi_2^2)^2. \tag{1.15}$$

Note that this is invariant under the global gauge transformation

$$\phi \rightarrow \phi' = e^{i\chi}\phi. \tag{1.16}$$

Now the minimum no longer occurs at two points but along a circle of radius $\phi_1^2 + \phi_2^2 = -\mu^2/\lambda = v^2$. Again, the procedure is to pick a point, breaking the symmetry, and then expand around it. Arbitrarily, we choose the point $\phi_1 = v$, $\phi_2 = 0$ and expand by η around ϕ_1 and ρ around ϕ_2:

$$\phi = \frac{(v + \eta + i\rho)}{\sqrt{2}}. \tag{1.17}$$

Substituting this back into the Lagrangian, we find

$$\mathcal{L} = \frac{1}{2}(\partial_\mu \rho)^2 + \frac{1}{2}(\partial_\mu \eta)^2 + \mu^2\eta^2 - \lambda^2 v(\eta\rho^2 + \eta^3) - \frac{\lambda^2}{2}\eta^2\rho^2 - \frac{\lambda^2}{4}\eta^4 - \frac{\lambda^2}{4}\rho^4 + constant. \tag{1.18}$$

Note that even though there are two fields, η and ρ, there's a mass term only for η. The field ρ describes a massless particle called a Goldstone boson. Whereas η obtains mass by excitations in the radial direction of the potential, ρ is associated with movement around the circle at the bottom of the potential. For this reason, the breaking of the symmetry leaves ρ massless and η with a mass term.

To apply this procedure to the vector fields of the Standard Model, we also have to examine the case of an SU(2) doublet Higgs field. For this doublet, we choose $\phi = \begin{pmatrix} \phi^+ & \phi^0 \end{pmatrix}$ where ϕ^+ and ϕ^0 are both complex fields:

$$\phi^+ = \frac{\phi_1 + i\phi_2}{\sqrt{2}}, \tag{1.19}$$

$$\phi^0 = \frac{\phi_3 + i\phi_4}{\sqrt{2}} \tag{1.20}$$

The Lagrangian still has the same form,

$$\mathcal{L}_\phi = T - V = (\partial_\mu \phi)^\dagger(\partial^\mu \phi) - (\mu^2\phi^\dagger\phi + \lambda^2(\phi^\dagger\phi)^2). \tag{1.21}$$

We can see that the potential energy component of this Lagrangian is invariant under the local SU(2) gauge transformation

$$\phi(x) \to \phi'(x) = e^{i\vec{\alpha}(x)\cdot\vec{\tau}/2}\phi(x) \tag{1.22}$$

where $\vec{\alpha}(x)$ is the phase shift and $\vec{\tau}$ is the set of Pauli spin matrices.

The minimum of the potential is now at

$$\phi^\dagger\phi = \frac{-\mu^2}{2\lambda^2} = \frac{v^2}{2}. \tag{1.23}$$

Again, we must choose a direction from which to expand around the minimum. Let's choose $\phi_3 = v$, $\phi_1 = \phi_2 = \phi_4 = 0$; so the expansion is

$$\phi = \frac{1}{\sqrt{2}}\begin{pmatrix} 0 \\ v + H(x) \end{pmatrix}. \tag{1.24}$$

Since we started with a doublet, but only one component has a vacuum expectation value, the SU(2) symmetry has been broken.

For the Lagrangian (both kinetic and potential energy parts) to be invariant under the local gauge transformation described above, we have to replace ∂_μ with the covariant derivative for U(1) X SU(2):

$$\mathcal{D}_\mu = \partial_\mu - ig_1\frac{Y}{2}B_\mu - ig_2\frac{\vec{\tau}}{2}\cdot\vec{W_\mu}. \tag{1.25}$$

The Lagrangian will now contain the terms

$$(\frac{1}{2}vg_2)^2 W_\mu^+ W^{-\mu} + \frac{1}{8}v^2(g_1 B_\mu - g_2 W_\mu^3)^2. \tag{1.26}$$

The first term depicts W self-interaction, giving the mass term $M_W = \frac{vg_2}{2}$.

It can be shown that the field for neutral current interactions is

$$Z_\mu = \frac{-g_1 B_\mu + g_2 W_\mu^3}{\sqrt{g_2^2 + g_1^2}}, \tag{1.27}$$

so the Z mass term should include

$$Z_\mu Z^\mu = \frac{(g_1 B_\mu - g_2 W_\mu^3)^2}{g_1^2 + g_2^2} \tag{1.28}$$

The second term in equation (1.26) has elements of this, from which we can conclude that $M_Z = \frac{1}{2}v\sqrt{g_1^2 + g_2^2}$. Note that there is no mass term for A_μ, so the mass of the photon is zero, as expected. With the inclusion of the Higgs mechanism, the W and Z bosons obtain mass while the photon remains massless.

1.4 Fermion masses

A similar procedure can be carried out to show that the inclusion of the Higgs field can provide masses for the fermions as well. Beginning with the leptons, the SU(2) invariant interaction term is added to the Lagrangian:

$$\mathcal{L}_{int} = g_e(\bar{L}\phi e_R^- + \phi^\dagger \overline{e_R^-} L) \tag{1.29}$$

where

$$L = \begin{pmatrix} \nu_e \\ e^- \end{pmatrix}_L \tag{1.30}$$

and

$$\phi = \begin{pmatrix} \phi^+ \\ \phi^0 \end{pmatrix}. \tag{1.31}$$

As before, the symmetry is broken by a choice of direction and an expansion is made around the minimum of the potential,

$$\phi \to \begin{pmatrix} 0 \\ \frac{v+H}{\sqrt{2}} \end{pmatrix}. \tag{1.32}$$

The interaction Lagrangian will now look like

$$\mathcal{L}_{int} = \frac{g_e v}{\sqrt{2}}(\bar{e}^-_L e^-_R + \bar{e}^-_R e^-_L) + \frac{g_e}{\sqrt{2}}(\bar{e}^-_L e^-_R + \bar{e}^-_R e^-_L)H. \tag{1.33}$$

The first term implies an electron mass, $m_e = \frac{g_e v}{\sqrt{2}}$, and an interaction strength for electron-Higgs coupling,

$$g_e = \frac{\sqrt{2} m_e}{v}. \tag{1.34}$$

It is very important to note that this interaction strength is directly proportional to the mass of the particle to which it is coupling. The Higgs will couple more strongly to heavier particles. The same calculation can be made for quarks, revealing the same relationship between interaction strength and the mass of the particle.

Summary

When calculated directly from the Proca and Dirac equations, all of the bosons and fermions are massless. By including the Higgs field and invoking spontaneous symmetry breaking, the fermions and gauge bosons that we expect to be massive acquire mass terms. Furthermore, the coupling strength of the Higgs boson to any particle is directly proportional to the mass of that particle. The mass of the Higgs itself, however, is not predicted by the theory, which means that the experimental search for it must be conducted over a range of mass hypotheses.

CHAPTER 2

Higgs Boson Production and Decay

2.1 Higgs Production

At the energies available to LEP2, the main mechanism of Higgs production is “Higgs-strahlung” ($e^+e^- \to Z^* \to hZ$) in which electron-positron annihilation produces an off-shell Z boson which then radiates a Higgs boson. This process is shown in the figure below.

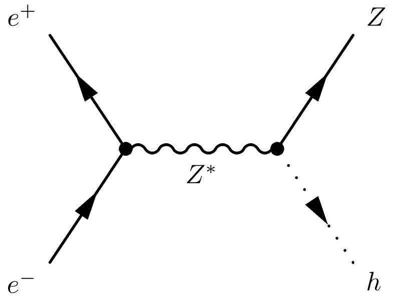

Figure 2.1. $e^+e^- \to Z^* \to hZ$

For Higgs-strahlung, the energy available to the Higgs is determined by the electron-positron beam energies. Energy conservation requires the total energies of the Z and Higgs plus any radiated photons to add up to the center-of-mass energy of the interaction ($\sqrt{s}$). Therefore, the Higgs may have energies up to $E_{cm} - E_Z$, where $E_Z = \sqrt{P_Z^2 + M_Z^2}$. In the most extreme case of the resultant Z boson having little or no momentum, the energy available to the Higgs will be $E_{cm} - M_Z$. There is some leeway here because the Z (nominal mass = 91.2 GeV) has a finite width: Γ_Z= 2.5 GeV, but the Higgs-strahlung cross section will drop sharply for Higgs masses just above $E_{cm} - M_Z$. This can be seen in figure 2.3. The lowest-order production cross-section for the Higgs-strahlung process is given by [2]

$$\sigma(e^+e^- \to hZ) = \frac{G_F^2 M_Z^4}{96\pi s}(v_e^2 + 1)\lambda^{1/2}\frac{\lambda + 12M_Z^2/s}{(1 - M_Z^2/s)^2}, \tag{2.1}$$

where G_F is the Fermi coupling constant, s is the center-of-mass squared, $v_e = -1 + 4\sin^2(\theta_W)$ (where θ_W is the weak mixing angle) and λ is defined by

$$\lambda = \frac{[1 - (m_h + M_Z)^2][1 - (m_h - M_Z)^2]}{s^2}. \tag{2.2}$$

Other possible mechanisms of Higgs production include WW-fusion: $e^+e^- \to W^{*+}W^{*-} \to h\nu_e\bar{\nu}_e$ and ZZ fusion: $e^+e^- \to Z^*Z^* \to he^+e^-$. The Feynman diagrams for these processes are shown below.

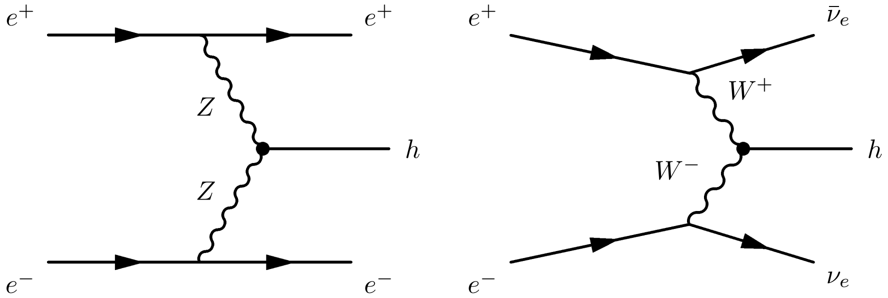

Figure 2.2. Feynman diagrams for Higgs production via ZZ and WW fusion processes, respectively.

Even at the highest LEP2 energy (209 GeV) the Higgs-strahlung cross section for a Higgs mass hypothesis of $m_h = 115$ GeV is at least five times larger than WW-fusion and fifty times larger than the cross-section for ZZ-fusion. For this reason, the analysis presented here is designed to search for the Higgs Boson via the Higgs-strahlung process.

2.2 Higgs Decay

The Higgs Boson is extremely short-lived: soon after production, it will decay into other particles. The main decay modes available to a Higgs boson that can be pro-

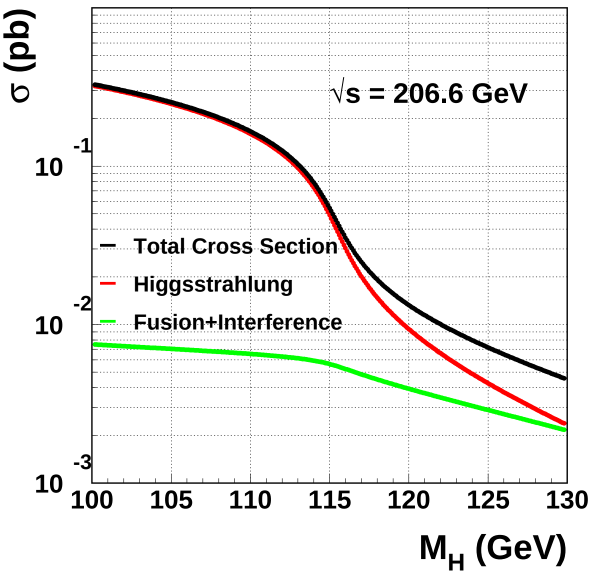

Figure 2.3. The Higgs production cross sections as a function of mass.

duced at LEP2 energies are quark decays ($h \to b\bar{b}$ and $c\bar{c}$), lepton decay ($h \to \tau^+\tau^-$), gluon decay ($h \to gg$) and W decay ($h \to WW^*$). In the previous chapter, it was shown that the Higgs coupling strengths are proportional to the masses of the particles to which it is coupled. Since the Higgs carries no flavor or charge, laws conserving these quantities require that a Higgs must decay into either a particle and its antiparticle or to other flavorless, neutrally charged (or oppositely charged) particles. Below $\sqrt{s} = 210$ GeV, a Higgs Boson created via the Higgstrahlung process (i.e. with a maximum of $E_{CM} - M_Z \leq 120$ GeV available) will most likely decay into a $b\bar{b}$ quark pair. Decays into tau or off-shell W Boson pairs are the next most likely modes but the branching ratios for these processes are about an order of magnitude less than for b-quarks. This is shown in figure 2.4.

Quark hadronization

The dominant decay mode of Higgs bosons produced at LEP2 energies is to a b-quark pair. These quarks, however, are not directly observed in our detectors. The quarks "hadronize" into particle jets which are observed.

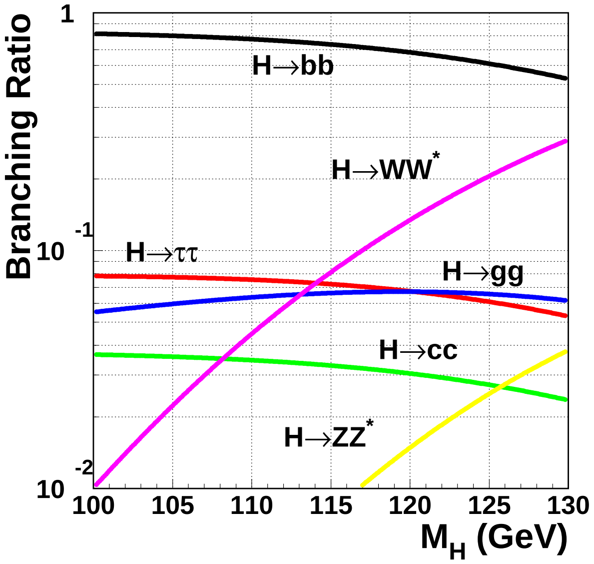

Figure 2.4. The relative branching ratios for Higgs decays.

It is a property of Quantum Chromodynamics (QCD) that quarks are always confined to hadrons. The gluon field between a quark and anti-quark is such that the potential energy increases as the distance between the pair grows. In the event of a quark and anti-quark moving in separate directions after a collision, the energy between them increases until there is enough to produce mesons. The process continues in this fashion and multiple hadrons are formed, preventing the appearance of a bare quark. Pions are commonly found in the hadron jets because they are relatively light and can be produced with less energy than other hadrons. The subsequent hadron jet is measured by the detector and the original energy and momentum of the quark is extracted. The early stage of hadronization when only a few particles have come from quark decay is used to determine the quark flavor in a technique called "b-tagging" which will be discussed in the next chapter.

2.3 The L3 Higgs Search Channels

Since the most dominant production and decay modes have been identified, the method of searching for the Higgs boson can begin to be defined. As was stated above, Higgs-strahlung is the leading method of production at the energies available at LEP2. In the accessible mass range, the Higgs boson usually decays into b-quark pairs, but the Z boson has several decay possibilities. It may decay into quarks, neutrinos, leptons ($l = e$ or μ) or taus with branching fractions of 0.70, 0.20, 0.07 (for e's and μ's combined) and 0.03, respectively. The leptons and taus are considered separately because their signatures are somewhat different and the tau channel is further complicated by a possible $h \rightarrow \tau^+\tau^-$ decay as discussed above. Each of the four channels has unique signal characteristics which tend to prevent overlapping analyses.

2.3.1 $hZ \rightarrow b\bar{b}q\bar{q}$

The $hZ \rightarrow b\bar{b}q\bar{q}$ channel is called the "4-jet" channel because this is nominally what one would expect to see from a signal. The Higgs decays into a b-quark pair and the Z decays hadronically as well, although no flavor for the Z decay is strongly preferred. The signature for this channel is four high multiplicity jets in which there are at least two jets coming from b-quarks. Because of the high branching fraction of Z Bosons into quark pairs, there will be a large number of events relative to the other channels. The Standard Model background events, however, are more difficult to distinguish from Higgs events, making this a relatively "dirty" channel.

2.3.2 $hZ \rightarrow b\bar{b}\nu\bar{\nu}$

In the interaction, $hZ \rightarrow b\bar{b}\nu\bar{\nu}$, the Higgs decays to a b-quark pair, while the Z decays to a neutrino pair. The ν's will not be detected as they interact very weakly with other particles. The signature of this channel is two jets, coming from b-quarks, large missing energy and missing mass consistent with the mass of the Z Boson. There are many fewer events expected in this channel because of the lower branching fraction for $Z \rightarrow \nu\bar{\nu}$. However, the Standard Model background events are easier to distinguish from signal events so this search is "cleaner" than the 4-jets search. The research described in this dissertation focusses on this channel, which will be discussed at length in the next chapters.

2.3.3 $hZ \rightarrow b\bar{b}l^+l^-$

In the cleanest lepton channels, the Higgs decays into a b-quark pair, and the Z decays into a pair of either electrons or muons. The signature, therefore, is two hadronic jets coming from b-quarks and a lepton pair with an invariant mass $\sim M_Z$. Because of the small branching fraction for $Z \rightarrow l^+l^-$, very few Higgs events are expected in this channel. The invariant mass of an electron or muon pair can be measured very accurately by the L3 detector so signal events are easily separated from background events as the Higgs mass hypothesis moves away from the Z mass. The lack of indistinguishable Standard Model background events at $M_h > 100$ GeV makes this the cleanest of the $e^+e^- \rightarrow hZ$ channels investigated.

2.3.4 Taus

The "tau" channel includes two distinct possible decays: $hZ \rightarrow b\bar{b}\tau^+\tau^-$ and $hZ \rightarrow \tau^+\tau^-q\bar{q}$. In the first case, the Higgs decays into a b-quark pair and the Z decays into a τ-lepton pair. In the latter, the Higgs decays into a τ-lepton pair, and the Z decays hadronically. The tau channels require the difficult task of tau identification. These heaviest of leptons decay quickly into either one charged particle (85 % of the time) or three charged particles, generally pions (15 % of the time) plus ≥ 0 π^0's. The mass resolution for the taus is generally worse than for the other lepton channels because the neutrinos in the τ decays will not be detected. The signature for $b\bar{b}\tau^+\tau^-$ is two hadronic jets coming from b-quarks and two taus with a mass consistent with M_Z. For $\tau^+\tau^-q\bar{q}$, the jets may stem from any flavor of quarks that have a combined energy consistent with that of a Z Boson decay. The tau channels are not as clean as the other lepton channels because the invariant mass of the τ's will not be as precisely measured.

CHAPTER 3

CERN, LEP and the L3 detector

3.1 Location and history

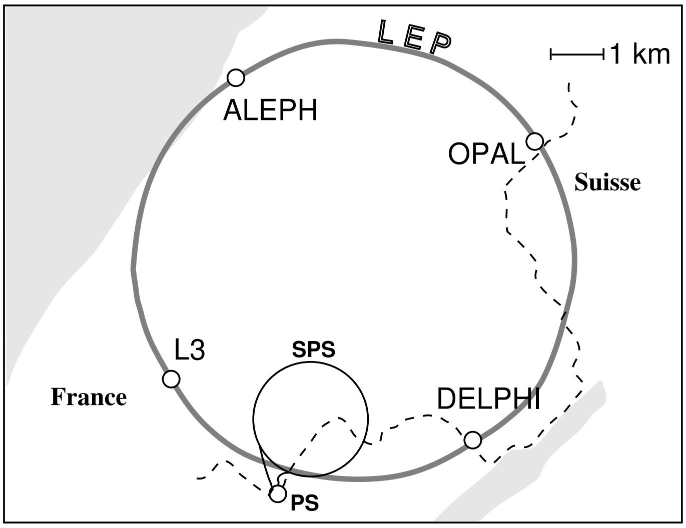

Figure 3.1. The geographical layout of the LEP collider as seen from above.

CERN, the European Center for Particle Physics, was founded in 1954 to be an international laboratory for the study of fundamental particles. The laboratory straddles the French-Swiss border just outside of Geneva, Switzerland. Throughout CERN's existence, it has housed a series of accelerators, each one progressing to higher and higher energies. In 1957, CERN's first accelerator, a 600 MeV proton Synchro-Cyclotron, began operation. Two years later, the 28 GeV Proton Synchrotron (PS) began its reign as the world's highest energy accelerator. In 1976, operation of the Super Proton Synchrotron (SPS) began. Among the important discoveries made by these machines were the observation of pion decay (Synchro-Cyclotron), the study of neutral current interactions with neutrinos (PS) and the discovery of the W and Z Bosons (SPS). Several Nobel Prizes have also been awarded based on work done at CERN. In 1981, the CERN management approved a plan to build the world's largest particle accelerator: the Large Electron-Positron (LEP) collider.

3.1.1 The LEP accelerator

Finished in 1989, LEP consists of a 27 km underground ring around which electrons and positrons are accelerated in opposite directions before colliding with each other head-on at predetermined points. That year, LEP (usually referred to as LEP1 before 1995) commenced operation with a center of mass energy (E_{CM}) near the mass of the Z boson ($M_Z \approx 91$ GeV) to perform precise measurements of this particle's properties. In 1995, LEP started running at higher energies with the eventual goal of studying the pair production of W Bosons (this period of LEP operation is referred to as LEP2). Since LEP2 began, the E_{CM} has been steadily increasing to a maximum of 209 GeV, achieved in the year 2000 (see table 3.1 for luminosity and center-of-mass of data taken in the year 2000). After the 2000 data taking period, LEP was shut down to make way for the Large Hadron Collider which is scheduled to begin taking data in 2006.

The PS and SPS machines are used to deliver 20 GeV electrons and positrons for injection into LEP. The LEP tunnel is split up into eight bending sections and eight straight sections. Electro-magnetic pulses, generated in superconducting radio frequency (RF) cavities, are used to accelerate the beam from the injection energy and to replace energy lost by synchrotron radiation. Over 3000 dipole magnets are used to bend the beam around the tunnel. In the straight sections, four of which house the detectors, superconducting quadropole magnets are used to compress the beam. The LEP accelerator uses two different bunching schemes for the particles as they make their way around the tunnel. For running at high energy, electrons and positrons are grouped in 2 × 4 bunches in the ring. The distance between the bunches is such that the difference in the time of potential collisions is 22 μs. For running at the Z peak, a "bunch train" scheme is used whereby the bunches are replaced by "trains" of up to four bunchlets that collide at time intervals as short as 250 ns.

3.2 The L3 experiment

Electron and positron bunches, accelerated to the high energies discussed above, are forced to collide at four separate points along the LEP ring. L3 is one of four general-purpose detectors situated at these interaction points. The name "L3" comes form the fact that it was the third experiment to submit its detector proposal to the CERN management. The other experiments are ALEPH, DELPHI and OPAL.

3.2.1 The mission

The L3 collaboration consists of over 500 scientists representing 49 institutes from all over the globe. The L3 collaboration's scientific mission is "to answer the most fundamental questions of physics by probing new energy regions. This exploration will endeavor to identify and study new physics phenomena not predicted by theory. By asking what are the basic building blocks of nature, how many quarks and leptons exist, and what is the origin of particle masses, new knowledge on the structure and nature of matter will be acquired."(The L3 Experiment: Progress in Physics, Technology and International Collaboration, October 1988)

3.2.2 The detector

The L3 detector is located at interaction point 2 along the LEP beamline. It is a layered combination of several subdetectors with the interaction region at its center (see figures 3.2 and 3.3). Each subdetector is designed to measure various properties of each "event" (e^+e^- collision). The L3 detector was designed to allow precise measurements of electrons, muons and photons. As such, certain elements of the

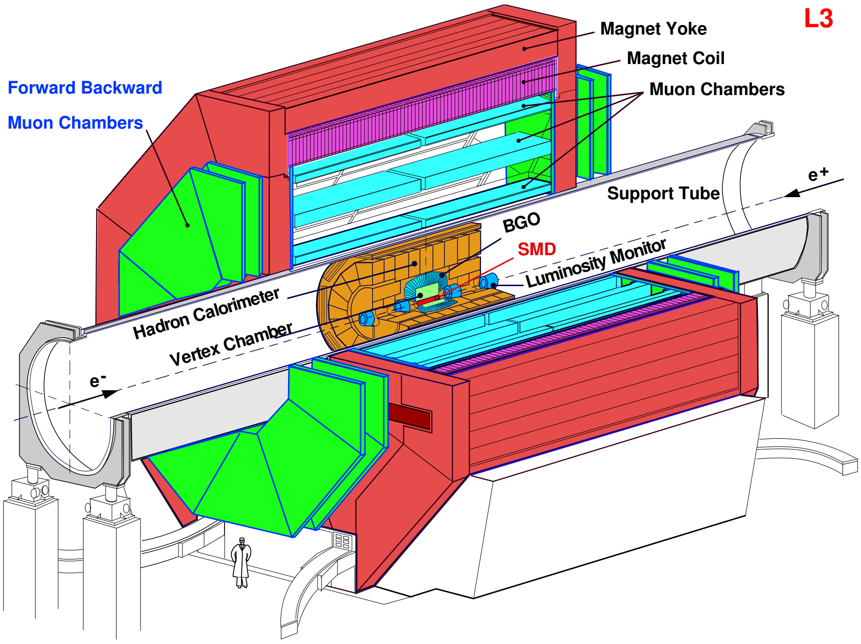

Figure 3.2. The L3 detector.

detector are emphasized in order to allow for higher resolution energy measurements of these particles. When a positron and electron interact in the middle of the detector, a host of possible particles are created. As these particles pass through the detector, properties such as their position, electric charge, energy and momentum are measured. In each interaction, the electronic signal outputs of each subdetector are combined and processed together in order to reconstruct the actual constituents of the event. Each subdetector has its own role, contributing to the understanding of an event.

The Magnet

The detector is situated within a large magnet, as shown in figure 3.2. The muon chambers are accessed via the large magnet doors on either end. The magnet has an outer radius of 7.9 m and an inner radius of 5.9 m. A current of 30,000 Amps is used to create a magnetic field of 0.5 Tesla. In 1994, an additional toroid was placed between the inner and outer radius of each magnet door. The magnetic field within the doors is 1.2 Tesla. The uniform field produced by this enormous solenoid bends the trajectory of charged particles, making their momenta and masses easily

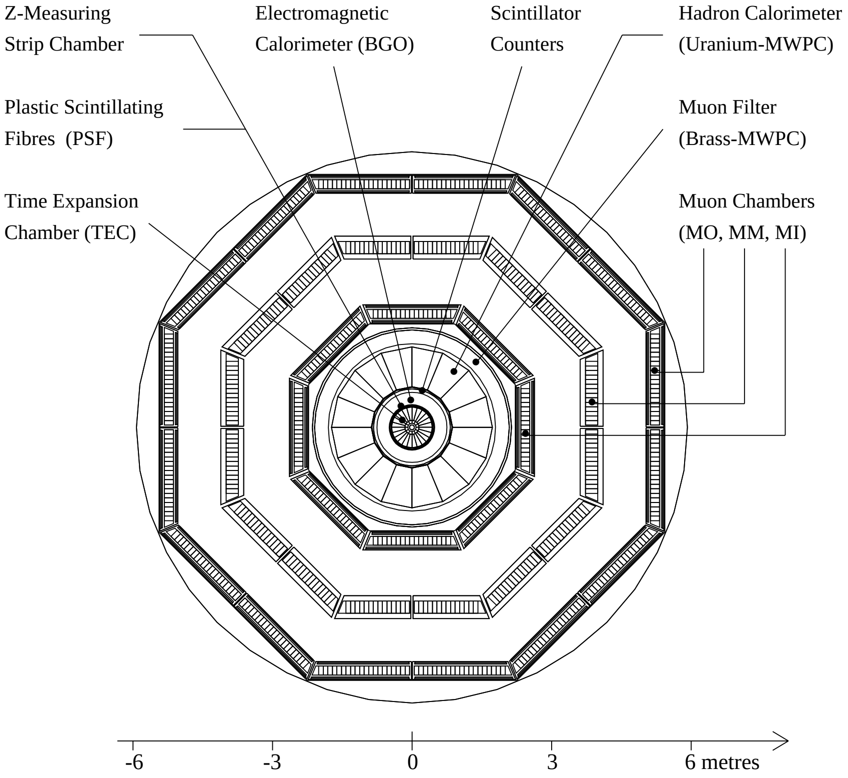

Figure 3.3. Cross section of the L3 subdetectors.

identifiable.

3.2.3 The Silicon Microvertex Detector

In 1991, the narrowing of the LEP beampipe from 8 cm to 5.5 cm allowed L3 to include a Silicon Microvertex Detector (SMD) [6]. This device is composed of two layers of double-sided silicon strip detectors which provide angular (ϕ) and longitudinal (z) measurements to an accuracy of 10 μm. The SMD covers an azimuthal range of $22^o < \theta < 158^o$. It's main function is to aid the tracker (see next section) in measuring the energy and momenta of jets. The SMD is especially useful for resolving secondary vertices which may arise from short-lived particles (e.g. hadrons containing b-quarks).

3.2.4 The Central Tracker

Surrounding the SMD, the central tracker measures the positions and momenta of charged particles (see figure 3.5. It has three components: a Time Expansion Cham-

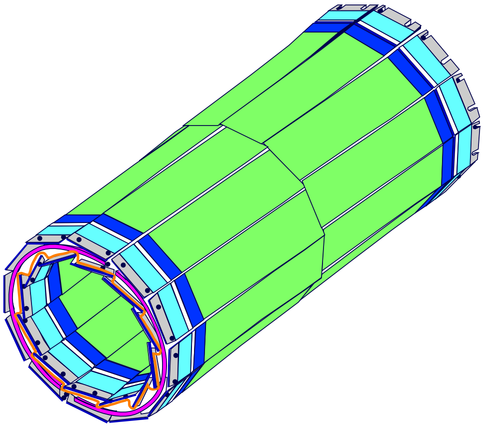

Figure 3.4. The silicon microvertex detector.

ber (TEC), a layer of scintillating fibers and the "z-detector". The TEC is composed of concentric cylindrical drift chambers, divided into 12 inner and 24 outer sections. The gas used in the chambers is a combination of 80% carbon dioxide and 20% isobutane, giving a drift velocity of 6 μm/ns. Each of the 24 outer sections is covered by a ribbon of 143 plastic scintillating fibers. The ribbon is used to measure the drift velocity of the gas within the TEC. This measurement is very important for properly evaluating the momenta of particles. The z-detector consists of two proportional chambers with a cathode strip readout. It supplements the TEC measurement of the z-coordinate with a resolution of about 320 μm.

3.2.5 The Electromagnetic Calorimeter

The next layer is the electromagnetic calorimeter (ECAL) which uses about 11,000 bismuth germanium oxide ($Bi_4Ge_3O_{12}$ or "BGO") crystals to precisely measure photons and electrons. The ECAL can measure the energy and position of these particles from 100 MeV to 100 GeV with a resolution of 5% at 100 MeV and less than 1% above 1 GeV. BGO is an attractive option for this subdetector because it has a high stopping power (i.e. short radiation length) for photons and electrons, low afterglow (allowing a quick reset between interactions) and it does not readily absorb moisture. Each crystal is a truncated pyramid that measures approximately 3 × 3 cm at the

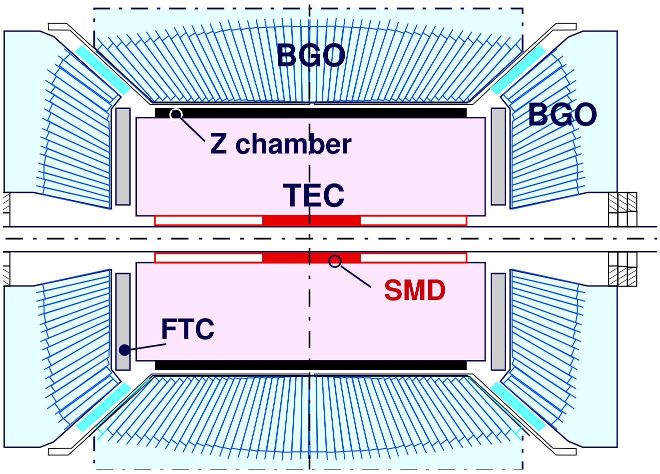

Figure 3.5. The TEC and electromagnetic calorimeter.

base, 2 × 2 cm at the top and 24 cm in length. The shape of each crystal is slightly different so that they all point into the interaction region, regardless of z-position. Actually, they are all slighty misalligned with the interaction point to avoid any loss that might arise from having particles sneak through the small cracks between them. Two photodiodes are glued to the rear face before the crystal is wrapped in Teflon tape and then copper foil. Transparency is monitored by a light pulse system to account for any radiation damage. The ECAL consists of two cylindrical half-barrels and two end-caps. The barrel region covers an azimuthal range $42^o < \theta < 138^o$. The end caps, added later, have an angular range of $11.6^o < \theta < 38^o$ and $142^o < \theta < 168.4^o$.

The Egap

In the azimuthal range $38^o < \theta < 42^o$ and $138^o < \theta < 142^o$ there is no coverage by the original electromagnetic calorimeter. In 1996, L3 filled this space with a lead-scintillating fiber calorimeter [7]. Lead modules, or "bricks" are filled with scintillating fibers pointing towards the intereaction point and placed in the ECAL gap. This is called a spaghetti calorimeter (SPACAL) because of the use of these long, thin fibers. The energy resolution in the SPACAL for an incident particle with energy, E, was found to be

$$\frac{\sigma(E)}{E} = (2.3 \pm 0.6)\% + \frac{(11.6 \pm 1.3)}{\sqrt{E(GeV)}}\%. \tag{3.1}$$

3.2.6 The Scintillation Counters

Between the ECAL and the HCAL, an array of scintillators helps prevent cosmic ray muons from being confused with dimuon events originating from the interaction point. The scintillation counters cover an azimuthal range of $25^o < \theta < 155^o$. Hits from cosmic ray muons are separate in time while those from a dimuon event are almost simultaneous.

3.2.7 The Hadron Calorimeter

A hadron calorimeter (HCAL) is used in conjunction with the ECAL to glean information about the energies and directions of hadronic jets. The HCAL uses a total absorption technique which also serves as a filter, allowing only non-showering particles to pass through to the muon detector. The HCAL consists of barrel and endcap components which cover the complete azimuthal range and polar range from $5.5^o < \theta < 174.5^o$. The barrel, covering $35^o < \theta < 145^o$, has 9 rings of 16 modules. Each module is made up of layers of 5 mm thick depleted Uranium interspersed with wire proportional chambers. The modules of the three innermost rings have 19 layers while the three on either side have only 17 layers. The proportional wire chambers are alternately placed perpendicular and parallel to the beam axis to allow for better determination of the particle trajectories. The perpendicular chambers measure the polar angle while the parallel ones measure the azimuthal angle. The endcaps consist of six half-rings on each side, filled with alternating layers of brass tube proportional chambers and absorber plates of depleted Uranium. The plates closest to the interaction point have been replaced with steel in order to shield the TEC and BGO from the radioactive Uranium. Uranium is used in the HCAL because it has a short absorption length. The radioactivity of the Uranium is also useful as a gamma source

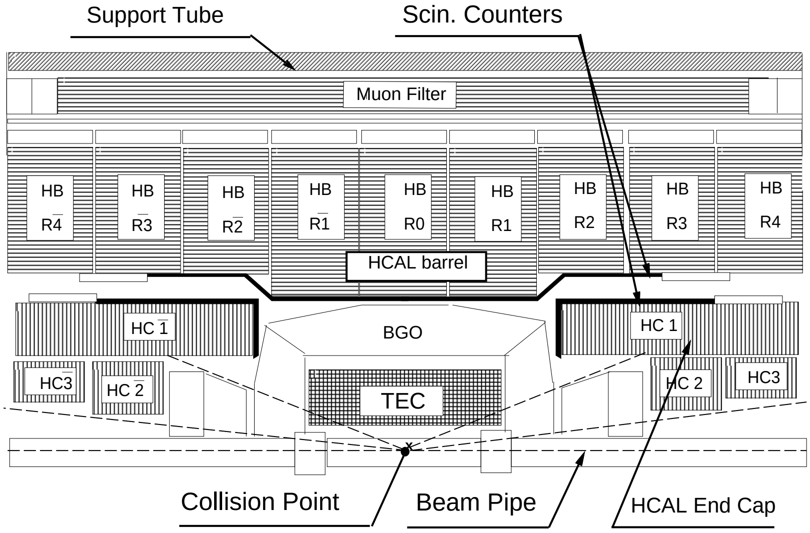

Figure 3.6. The hadron calorimeter.

for calibrating the the wire chambers. Surrounding the HCAL is the muon filter: five proportional wire chambers are interleaved with six layers of 1 cm thick brass plates and then five layers of 1.5 cm thick brass plates. The muon filter is a preventative measure to ensure that no hadrons enter the muon chambers.

3.2.8 The Muon Chambers

Enveloping the rest of the detector, three layers of large drift chambers precisely detect and measure muons. The muon chambers are segmented such that there is a barrel component and forward-backward components. The barrel chambers consist of eight octants of five precision drift (P) chambers each, located on either side of the intersection point.

The five chambers of each octant are divided into three layers. The innermost (MI) has one chamber with 16 wires, the middle one (MM) has two chambers with 24 wires apiece and the outermost (MO) has two chambers of 16 wires apiece. The P chambers measure track coordinates in the bending plane. Atop the MI and MO layers, there are additional six "Z" chambers per octant that measure the z coordinate

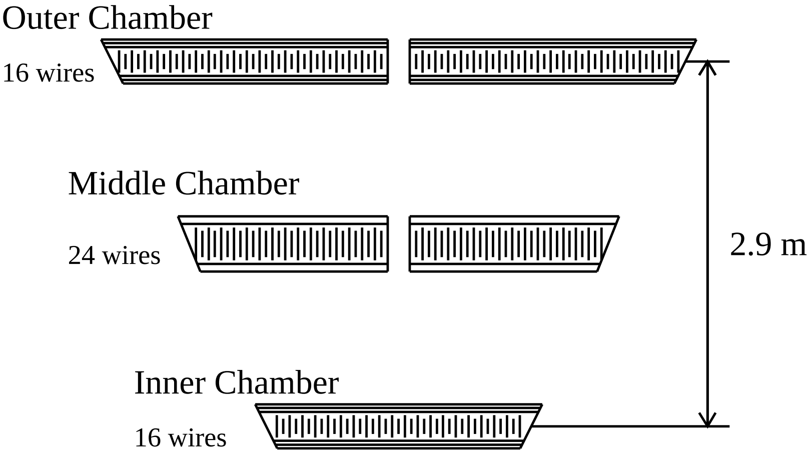

Figure 3.7. Cross section of a muon chamber octant.

of the passing particle. In combination, the P and Z chambers measure the position and momentum of muon by the curvature of its path in the magnetic field. The 0.5 Tesla magnetic field will induce a 50 GeV muon to deviate from its original path by a sagitta of 3.4 mm. To achieve a mass resolution of 1.4%, the sagitta must be measured to within 70 μm. This is the accuracy to which the muon chambers were designed. The muon chambers are aligned using a system of LED's focused by a lens in the middle chamber. A nitrogen UV laser simulates a particle with infinite momentum whose sagitta should therefore be zero. Measuring this verifies the alignment of the chambers. Muon chambers in the forward and aft portions of the detector were added in 1995. They had to be placed around the magnet doors because they were added long after the magnet was in place. As in the barrel muon chambers, there are three layers of drift chambers. The innermost layer (FI) is within the magnet door and the other two (FM and FO) are outside. The outer side of the FM layer and the inner side of the FO layer have resistive plate counters (RPC) for triggering. The forward-backward (FB) chambers cover two regions denoted S (solenoid) and T (toroid). The T region, $24^o < \theta < 36^o$ is defined as the range for which a muon may pass through all three FB chambers. The S region, $36^o < \theta < 44^o$ is defined as the range for which a muon may pass through the inner and middle barrel chambers as well as the inner FB chamber. At angles larger than 44^o, all three barrel chambers will be accessible to the muon. The alignment of the FB chambers is hampered by the motion of the magnet doors, making them much less precise than the barrel chambers. In addition, multiple scattering of muons in the steel doors precludes a momentum resolution better than about 30%.

3.2.9 The Luminosity Monitor

Forward and aft of the interaction point are two components of the luminosity monitor [8]. This device is used to keep track of the rate of electron-positron collisions as well as to study two photon interactions. Proportional chambers are used to measure the tracks of charged particles, and BGO crystals measure the energy of electromagnetic interactions. The luminosity is calculated by counting the number of small angle Bhabha events ($e^+e^- \to e^+e^-(\gamma)$. The cross section of these events is a well known quantity. The polar angular coverage of the luminosity monitor is 30 mrad $< \theta <$ 62 mrad, on both sides.

3.2.10 The Trigger

The information output from the subdetectors must be sorted so that only relevant events are recorded. To this end, a three-tiered trigger system is established [9]. The level-1 trigger has five subtriggers, one apiece for the calorimeters (electronic and hadronic), luminosity monitors, scintillation counters, muon chambers and the TEC chamber. The beam crossing signal is used as a gate for each of them. Each of the subdetector triggers is designed so that events that are deemed “interesting” will pass easily. If all five triggers have a negative result, then the electronics are cleared and the system will await the next beam crossing signal. If any one of the five gives a positive result, the fine digitization electronics will begin and the the event will move on to the second trigger level.

The level-2 trigger, given a smaller sample of events than the previous trigger, may take a longer look at them. The extra time allows for the cross-referencing of subdetector signals. This helps to remove unwanted calorimeter triggers caused by noise or TEC triggers caused by beam-gas, beam-wall interactions and synchrotron radiation. Events that satisify more than one level-1 trigger criteria, automatically pass the level-2 trigger.

The level-3 trigger consists of several possible algorithms. The choice of which to use for each event depends on which level-1 trigger selected the event. Each algorithm imposes more stringent criteria on the events to ensure that that event will be useful in the analyses. For example, events that pass the TEC trigger will be examined to see if their tracks have a common vertex and can be correlated with more than 100 MeV of energy in the calorimeters. If an event has passed multiple level-1 triggers, it will not be rejected by the level-3 trigger. This is the case for most interesting events.

3.2.11 Monte Carlo Production

There are several Standard Model (SM) processes which can appear like and swamp a possible Higgs signal. In order to see a statistically significant Higgs signal, we develop a systematic way of reducing these background events while maintaining as much of the Higgs signature as possible. To this end, Monte Carlo simulations are generated of background as well as signal (i.e. Higgs) processes. The analysis procedure is to use these simulations to find a way to cut away background events while keeping signal events.

The PYTHIA [10] program is used to simulate Higgs signal events. The SM background event samples are generated using PYTHIA ($e^+e^- \to ZZ, Ze^+e^-$), KK2F [11] ($e^+e^- \to q\bar{q}(\gamma)$), KORALW [12] ($e^+e^- \to W^+W^-$), EXCALIBUR [13] ($e^+e^- \to q\bar{q}'e\nu_e$) and PHOJET [14] ($e^+e^- \to e^+e^-q\bar{q}$).

Because we're dealing with small numbers of expected signal events, statistical fluctuations in the signal and background event samples can have a serious effect on the analyses. To avoid this problem, large numbers of Monte Carlo events are generated, thereby reducing these potentially problematic fluctuations.

The L3 detector's performance is simulated by GEANT [15] and GHEISHA [16]; the former takes into account the effects of multiple scattering, energy loss and showering inside the detector while the latter is used to simulate hadronic interactions.

3.2.12 b-tagging

As previously discussed, the dominant decay mode for Higgs bosons at LEP2 is to b-quarks. However, the background Standard Model processes (to be discussed later in this work) don't favor any particular quark flavor. Therefore in conducting a Higgs search, it is imperative to discern hadronic events containing b-quarks. This technique is called "b-tagging" because we'd like to essentially "tag" those events containing b-quarks. A performant b-tagging routine will enable the analyst to separate Higgs events from some SM background processes, providing for a cleaner, less ambiguous signal.

The average lifetime of hadrons containing b quarks is 1.5 picoseconds [2]. So at LEP energies, they typically travel a few millimeters before decaying into secondary hadrons with trajectories that can, ideally, be distinguished from those of primary hadrons originating from the interaction point. A small but non-negligible background comes from events with primary charm quarks, the average lifetime of which is about 1.0 picoseconds. By using the precise SMD, with a 5.3 cm radius, it is possible to trace the origin of the quark decays. If the reconstructed intersection of a subset of the tracks is displaced from the interaction point, forming a secondary vertex, the jet is likely to have been produced by a b-quarks. This lifetime information about the jet is crucial to the b-tag, all the other variables used give slight performance increases. A neural network [20] is created using secondary vertex information, jet shape variables, lepton identification and the polar angle of the jet. The output of this network is used as a jet b-tag. The two jet tags can then be combined to form an overall event b-tag. The tracking and b-tag performances in the Monte Carlo are tuned using 4 pb^{-1} of data taken for calibration purposes at $\sqrt{s} \sim m_Z$ in the year 2000.

3.3 Luminosity collected

The data sample used in this analysis was collected during the LEP year 2000 data run. A total integrated luminosity of 217.3 pb^{-1} was collected at center-of-mass energies ranging from 200 GeV to 209 GeV. The data was broken up into nine energy bins for analysis. These nine bins were then grouped to allow for the sharing of some Monte Carlo events among bins. The Monte Carlo used was generated at center-of-masses matching the mean E_{CM}'s in each luminosity bin. The binning and grouping is shown in table 3.1. Systematic uncertainties introduced by finite Monte Carlo samples at discrete center-of-mass energies will be discussed in chapter 5.

$\sqrt{s}$ range (GeV)	lumi. collected (pb^{-1})	mean E_{CM}	MC used for bkgd/sgnl (GeV)
199.5-200.5	0.67	199.8	202/202
201.501-202.5	0.58	201.8	
202.501-203.5	1.50	202.7	
203.501-204.5	7.61	203.8	204/204
204.501-205.5	68.10	205.1	205.1-206/205.1
205.501-206.5	67.01	206.3	206.6/206.3
206.501-207.5	63.54	206.6	206.6/206.6
207.501-208.5	8.16	208.0	208/208.2
208.501-209.5	0.09	208.6	

Table 3.1. Luminosity bins for data collected in the year 2000.

CHAPTER 4

Search in $hZ \rightarrow b\bar{b}\nu\bar{\nu}$

4.1 Topology

The process, $hZ \rightarrow b\bar{b}\nu\bar{\nu}$, is generally called the “missing energy” channel. This is no misnomer: neutrinos are notoriously non-interactive, so they slip through the L3 detector unnoticed. The neutrinos in this channel are decay products of a Z boson, so the missing mass of a signal event should be close to the Z mass. As stated in the previous section, we're also looking for $h \rightarrow b\bar{b}$, so two jets coming from b-quarks are expected. In addition, because the region being probed is just below the kinematic limit, not much kinetic energy is available to the Higgs. Therefore, it will decay very close to rest, giving the jets a back-to-back structure. More specific criteria for discriminating signal topology from SM background are described in the following sections.

4.2 Relevant Backgrounds

Many Standard Model processes occur in the e^+e^- interactions at LEP. Several L3 working groups are dedicated to the study of these interactions. These analyses are essential to any new particle search as they confirm our understanding of the background interactions and help us to troubleshoot detector problems. Accurate modelling of these backgrounds in our Monte Carlo simulations is necessary to our Higgs analyses. They help us to determine how background-like each data event is.

The dominant backgrounds to the missing energy Higgs analysis at the current

LEP2 energies are: two-photon ($e^+e^- \to e^+e^-q\bar{q}$), quark pair-production (($e^+e^- \to q\bar{q}(\gamma)$ and $q\bar{q}(\gamma\gamma)$), W pair-production ($e^+e^- \to W^+W^-$), single W production ($e^+e^- \to q\bar{q}'e\nu_e$), Z pair-production ($e^+e^- \to ZZ$) and single Z production ($e^+e^- \to Ze^+e^-$). The cross-sections for these backgrounds at a center of mass energy representative of the year 2000 running of LEP (E_{CM} = 206 GeV) are shown in table 4.1.

Background process	Cross-section (pb) @ E_{CM} = 206 GeV
Two photon	4.7×10^3
$q\bar{q}$	81.5
W^+W^-	17.5
$qq'e\nu_e$	3.23
ZZ	1.32
Ze^+e^-	3.58

Table 4.1. SM Background Cross Sections.

Although the two-photon background has a relatively enormous cross-section, it is very easily distinguished from the missing energy Higgs signal (as will be explained in the preselection section). The Standard Model backgrounds that are most difficult to distinguish from this search channel are ZZ and $q\bar{q}$.

4.2.1 The ZZ background

The ZZ background process has the Feynman diagram shown in figure 4.1. Each of the fermion pairs can be either quarks, neutrinos or charged leptons, giving a total of six unique final state combinations ($ZZ \to q\bar{q}q'\bar{q}', q\bar{q}l\bar{l}, q\bar{q}\nu_l\bar{\nu}_l, l\bar{l}l'\bar{l}', l\bar{l}\nu_{l'}\bar{\nu}_{l'}$ and $\nu_l\bar{\nu}_l\nu_{l'}\bar{\nu}_l'$).

If one of the Z bosons decays to neutrinos and the other goes to b-quarks ($ZZ \to b\bar{b}\nu_l\bar{\nu}_l$), the end products of this process will look just like those from the Higgs missing energy channel. The detector will see only two hadronic jets with a high b-tag and a large amount of missing energy. The branching fraction for this ZZ final state is

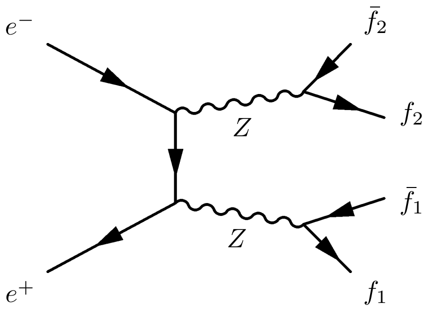

Figure 4.1. $e^+e^- \to ZZ \to f_1\bar{f}_1f_2\bar{f}_2$.

$$B_{b\bar{b}\nu\bar{\nu}} = B_{Z\to b\bar{b}} \times B_{Z\to\nu\bar{\nu}} = 0.03 \tag{4.1}$$

The distinguishing feature of this background is the narrow width of the Z mass. The mass of the two-jet system will be close to that of the Z ($M_Z \approx 91.2$ GeV, with a full-width-at-half-maximum spread of 2.5 GeV) whereas for the signal, the jets should be close to whatever Higgs mass is being investigated. As the probed Higgs mass region gets further from the Z mass, the signal becomes easier to distinguish from this background. However, there remains an irreducible, albeit infrequent, background of off-shell Z's that mimic a heavy Higgs boson. In the most signal-like region of the final discriminant (to be defined later) for $m_h = 115$ GeV, the ZZ background accounts for roughly 30% of the total background.

4.2.2 The $q\bar{q}$ background

The $q\bar{q}(\gamma)$ background has the Feynman diagram shown in figure 4.2.

In this process, one of the incoming particles emits a photon. The subsequent electron-positron interaction produces a virtual Z or γ which then decays into a quark pair. If the radiated photon is highly energetic, but not detected, this will look much like a missing energy Higgs signal. Although the emission of these highly energetic photons is disfavored, it is still possible for the emitted photon to carry away enough energy that a real Z boson, not a virtual one is produced. This is known as

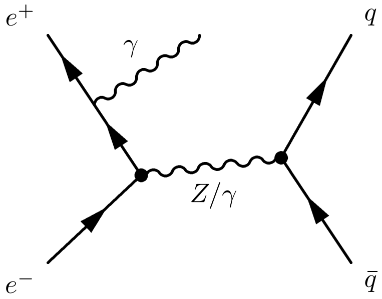

Figure 4.2. $e^+e^- \rightarrow q\bar{q}(\gamma)$.

the “radiative return to the Z”. There are events where the photon is undetected, usually because it escapes down the beam pipe. In these cases, the two jet final state can look like signal, especially if they come from a b-quark pair.

The most dangerous form of $q\bar{q}$ background is the double radiative return to the Z. In this process (shown in figure 4.3), a photon is emitted by both incoming particles so the Z Boson can be created on-shell with low total momentum.

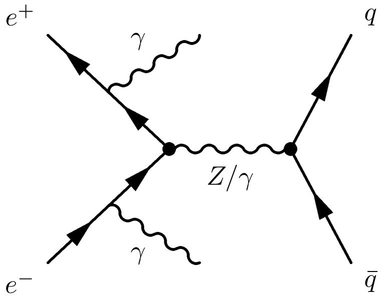

Figure 4.3. $e^+e^- \rightarrow q\bar{q}(\gamma\gamma)$.

There can be situations when both radiated photons are of similar energies so that there is no energy imbalance. These photons will most likely escape down the beampipe so there will be balanced missing energy. If the Z then decays to b-quarks, this will mimic the topology for the missing energy Higgs channel. The missing mass will be $M_{missing} \approx E_{CM} - M_Z$ while the invariant mass of the jets will be $\sim M_Z$. The analysis that will be presented in the next chapter employs a routine that fits the missing mass to the Z mass and then calculates the invariant mass of the quark pair based on the raw energies measured by the detector. The invariant mass calculated is then used as a hypothetical Higgs mass in the rest of the analysis. In collisions of $\sqrt{s}$=207 GeV, the missing mass is forced to be close to the Z mass, so the hypothetical Higgs mass will be around 115 GeV. The double radiative process, although rare, is an irreducible background in the most signal-like region. The total $q\bar{q}$ background represents roughly 70% of the most signal-like background for $m_h = 115$ GeV.

4.2.3 W pair background

The Feynman diagrams for W boson pair production are shown in figure 4.4.

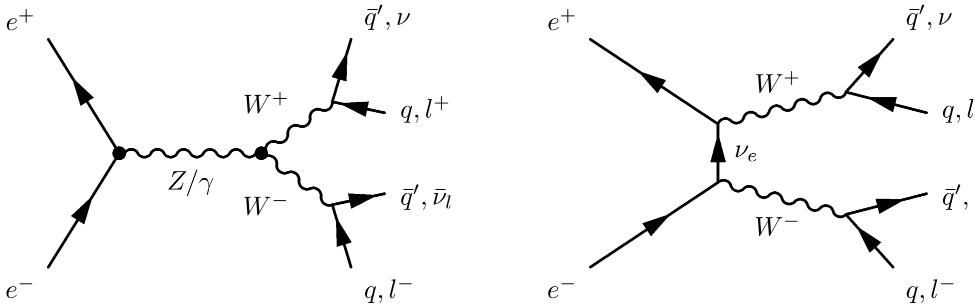

Figure 4.4. W pair production.

The most problematic W^+W^- background for the missing energy Higgs search is $W^+W^- \rightarrow q\bar{q}'l\bar{\nu}_l$. Although a single, isolated lepton is not part of the Higgs signal, it is possible for the lepton to go undetected either by being mistaken for part of a jet, slipping through a crack in the detector or escaping down the beampipe. If any of these were to happen, the result would be two hadronic jets plus missing energy. If the lepton were mistakenly included in a jet, one jet would probably account for much more energy in the event than the other and the two, together, would constitute a large fraction of the center-of-mass energy. If the lepton simply goes undetected, the two jets will probably be of roughly the same energy, adding up to the mass of the W boson. Because of the infrequency of these occurences, the unlikeliness of a high b-tag and the fact that we are conducting our search far from the W mass peak, the

WW background hardly contributes to the most signal-like background.

4.2.4 Single W background

The Feynman diagram for the single W Boson background is shown in figure 4.5.

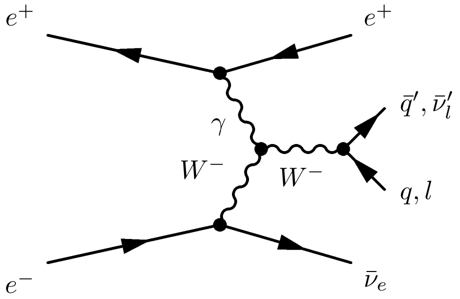

Figure 4.5. Single W production.

The signature of this background is just like that of the $W^+W^- \rightarrow q\bar{q}'l\bar{\nu}_l$ background except that here electrons and their neutrinos are the only lepton flavor produced. Still, the topology will be similar to W^+W^- production. This background also does not contribute significantly to the most signal-like background.

4.2.5 Zee background

The Feynman diagram for the Zee background process is shown in figure 4.6. In this diagram, the electron and positron are interchangeable.

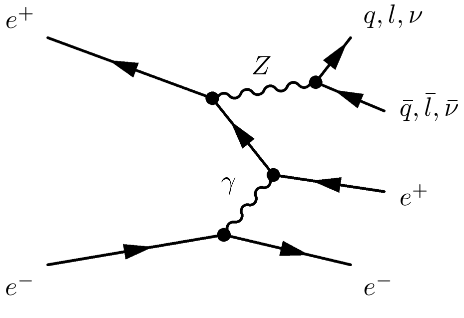

Figure 4.6. The Ze^+e^- background.

In the final state, there is an electron-positron pair and the Z boson can decay into hadrons, leptons or neutrinos. The most signal-like of these decays is the hadronic case. The $q\bar{q}e^+e^-$ final state will have two jets and two electron-like particles (the signature of the positron is the same as that of the electron, only the track bends the opposite way in the magnetic field). The two jets will have an invariant mass close to the Z and probably have enough momentum to not be back-to-back. This process could be mistaken for signal if the electron and positron are both within jets or undetected. The radiated Z Boson would also have to be far off-shell in order to have an invariant mass in the region of the search. These are both rare cases and because of this and the low cross-section for Ze^+e^-, it doesn't contribute significantly to the most signal-like background.

4.2.6 Two photon processes

The total cross section of two-photon processes is orders of magnitude larger than any of the other backgrounds, suggesting the possibility of a large contamination. The main Feynman diagram for this background is shown in figure 4.7.

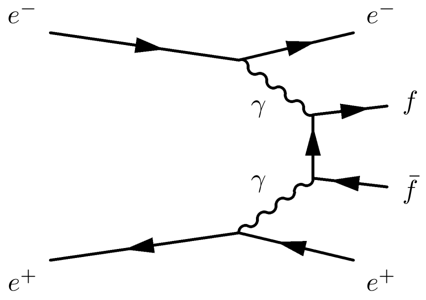

Figure 4.7. The 2 photon background.

The electron-positron pair usually scatter at very low angles. This means that they'll be lost down the beampipe (or, on very rare occasions, one may be incident upon the luminosity monitor). With these particles not accounted for in the detector, the event will certainly have a large amount of missing energy. In these instances, the missing momentum vector will be at a very low polar angle (i.e. close to the beampipe). There will be cases in which both electron and positron lose the same amount of energy and are deflected back-to-back, giving the event's missing momentum vector a larger polar angle, but this is an extremely rare phenomenon. Two photon processes typically have low visible energy and large momentum imbalance which easily distinguish these events from signal events. In fact, this background can be eliminated entirely from the data sample by a few requirements in the preselection. For this reason, the background due to two-photon processes does not contribute at all to the collection of Standard Model backgrounds to the missing energy Higgs search.

CHAPTER 5

Analysis

5.1 Analysis Procedure

The analysis procedure is to reduce the Standard Model backgrounds while retaining a large fraction of any Higgs signal that might be present. To do this, we find variables that provide discrimination between background and signal. The analysis is a three step process. In the first step, the preselection phase, cuts on individual variables are used to remove large quantities of backgrounds that are easily recognizable as not coming from signal. This will reduce the sample of events to a manageable quantity with which one can proceed. The second step involves the use of an artificial neural network [24] to generate an output variable that has excellent distinction between background and signal. The output of the neural network is combined with the reconstructed Higgs mass to form a final discriminant variable which will provide the most separation between Standard Model background and Higgs signal.

5.1.1 Preselection

The preselection requirements, used to remove obvious background events are very loose. They are applied regardless of assumed Higgs mass value and center-of-mass energy of the data. Examples of backgrounds that are virtually eliminated in this phase are Bhabha scattering ($e^+e^- \to e^+e^-$), leptonic two fermion final states, beam-gas interaction, cosmic rays and hadronic two-photon events ($e^+e^- \to e^+e^-q\bar{q}$). In addition, the other backgrounds are also reduced drastically by the preselection. The preselection requirements are:

- Hadronic event selection
    - number of tracks ≥ 4
    - number of asrc's > 15

An asrc ("A Smallest Resolvable Cluster") is derived from the combined energy deposits in the ECAL and HCAL. Minimum numbers of tracks and clusters are required to select hadronic events.

- Energy requirements
    - 5 GeV $\leq E_{ECAL} \leq$ 85 GeV
    - $E_{ECAL} + E_{HCAL} \geq 30\%$ of the visible energy
    - $E_{25^o} <$ 50 GeV

Demands on the energy deposited in the ECAL and HCAL select events that include moderately energetic hadronic jets. The E_{25^o} variable is the calorimeter energy within a 25^o cone around the missing momentum vector.

- Event shape variables
    - acollinearity $\geq$ 2.0 radians
    - maximum jet mass $\leq$ 70 GeV
    - minimum jet mass $\geq$ 2 GeV
    - $E_\gamma <$ 20 GeV
    - $|\text{cosine}(\theta_{P_{missing}})| \leq 0.96$
    - $|\text{cosine}(\theta_{thrust})| \leq 0.96$

Acollinearity is the angle between the jets. The acollinearity requirement ensures that the quarks' parent particle has relatively low momentum. Restrictions on the mass of the jets produced by the DURHAM algorithm tend to eliminate the leptonic two fermion final states, as well as suppress rare two-photon events where the electrons scatter at larger angles. The thrust axis is defined as $\hat{n}$ such that

$$T = \frac{\sum_i |\mathbf{n} \cdot \mathbf{p_i}|}{\sum_i |\mathbf{p_i}|} \tag{5.1}$$

(where $\mathbf{p}_i$ is the momentum vector associated with each particle) is a maximum[10]. The restrictions on the direction of the missing momentum vector and the thrust and the photon energy restriction reduce the $q\bar{q}$ background and virtually eliminate the two-photon background.

- Kinematic requirements
  - 40 GeV $\leq$ visible mass $\leq$ 140 GeV
  - 50 GeV $\leq$ missing mass $\leq$ 130 GeV
  - longitudinal missing momentum $\leq$ 60% of the visible energy
  - missing momentum $<$ 50 GeV

The visible mass is deduced from energy and momentum information gleaned from the energy deposits and tracks in the detector. In $q\bar{q}$ events where there is no radiative return ($e^+e^- \to q\bar{q}$), all of the center-of-mass energy is available to the visible mass. Such events can be removed by setting an upper limit on the amount of visible mass seen by the detector. The missing mass, defined as

$$M_{missing} = \sqrt{(E_{cm} - E_{vis})^2 - p^2_{missing}}, \tag{5.2}$$

is used to reduce events with a large fraction of energy in the detector. The magnitude and direction of the missing momentum vector are deduced from energy and momentum conservation. For the Higgs signal, the missing mass is expected to be near M_Z. The loose cuts implemented here remove events far from this benchmark. WW-pair production events are reduced by requirements on the maximum visible mass and the mass recoiled from the hadron system (missing mass). The ZZ background can be significantly suppressed in high Higgs mass search regions by cutting on the maximum missing momentum allowed. For a heavy Higgs (close to the kinematic limit) hypothesis, very little energy is available to go into the momentum; whereas in the

ZZ process, one of the Z pair would have to be very off-shell in order for the particles to decay at rest. Therefore, the Higgs events will, in general, have lower missing momenta.

- other requirements
  - $E_{lumi} + E_{alr} \leq 20$ GeV
  - event b-tag variable > 0.5
  - $|\text{cosine}(\theta_{j1})| > 0.97$

Two photon ($e^+e^- \rightarrow e^+e^-q\bar{q}$) events tend to leave a sizable amount of energy in the luminosity monitor and associated lead ring (ALR), so a maximum cut on $E_{lumi}+E_{alr}$ is required. There is a loose requirement on the b-tag variable (described in detail in section 3.2.12) that removes a large quantity of every type of background. The condition on the polar angle of a jet ($|\text{cosine}(\theta_{j1})|$) is implemented to ensure that events aren't included that have a high energy jet very close to the beampipe. If a jet is close to the beampipe, some energy could be lost at low angles and an event could survive with a jet whose energy is not properly measured.

These requirements are designed to exclude events with topologies very different from the missing energy Higgs signature. After the preselection process, the signal efficiency is about 71% while the estimated backgrounds have been greatly reduced (see table 5.1).

The remaining background events are mostly $q\bar{q}$ and W^+W^-. The ZZ and $qq'e\nu_e$ processes are responsible for a smaller fraction of the total Standard Model background at this stage.

5.1.2 The Reconstructed Higgs Mass

To search for evidence of the Higgs boson over a range of hypothetical masses, we need to reconstruct a best estimate of the Higgs mass for each event. This is done

Process	below $\sqrt{s} = 205.5$ GeV	above $\sqrt{s} = 205.5$ GeV
$q\bar{q}$	14.40	24.31
ZZ	6.44	10.75
W^+W^-	19.18	36.48
$q\bar{q}'e\nu_e$	6.32	11.31
Ze^+e^-	0.42	0.63
total	46.76	83.48
$hZ \to b\bar{b}\nu\bar{\nu}$ (m_h = 105 GeV)	2.17	4.11
$hZ \to b\bar{b}\nu\bar{\nu}$ (m_h = 110 GeV)	1.19	2.61
$hZ \to b\bar{b}\nu\bar{\nu}$ (m_h = 115 GeV)	0.21	0.73
Data	39	82

Table 5.1. Estimated numbers of background, signal and data events after preselection.

by using a kinematic fit routine that assumes that the two jets come from a Higgs that has recoiled off of a Z boson. The measured quantities in the fit are the energies and positions of the two jets. The Z mass, having a finite measured width, is allowed to vary according to a function based on a study of the jet resolutions [21]. The routine finds the most likely mass of a Higgs as well as the jet energies and total momentum. These can, and usually will, be different from those measured in the detector. The assumption of a Z boson recoiling from the jet-jet system will alter the invariant mass of that system. This is even true for the signal Monte Carlo. In figure 5.1, the distribution of fitted Higgs mass (m_h^{rec}) is shown for a 115 GeV Higgs boson hypothesis. The signal Monte Carlo peaks at about 114 GeV because of the influence of the kinematic limit ($E_{CM} - M_Z$). This shift is an important phenomenon because m_h^{rec} is used to create the final discriminant variable. A data event with m_h^{rec}=114 GeV will end up with a higher weight than one with m_h^{rec}=115 GeV, for an assumed true mass of 115 GeV.

The $q\bar{q}$ background is most likely to have an invariant mass of the jets near the center-of-mass energy (and therefore excluded by the preselection cuts) for no radiative return to the Z and another peak near 90 GeV with single or double radiative return to the Z. However, the kinematic fit automatically assumes that the jets are recoiling off of a Z boson and will use this to derive a most likely mass. The fit will be constrained by the measured jet energies and invariant mass, but it may still reconstruct the mass much higher than the measured value. A radiative return event with a true invariant mass of, say, 100 GeV, as measured by the detector, may have a reconstructed Higgs mass much closer to the kinematic limit. This is problematic because, as we can see in figure 5.1, the $q\bar{q}$ distribution peaks in the same region as the signal. The m_h^{rec} distribution, while excellent for discriminating signal from ZZ, W^+W^- and $q\bar{q}'e\nu_e$ backgrounds, is very poor when asked to do the same for the $q\bar{q}$ background. As will be shown later, some of the neural network input variables discriminate against events whose measured mass or jet energies are far from the fitted value. This will help subdue the $q\bar{q}$ background.

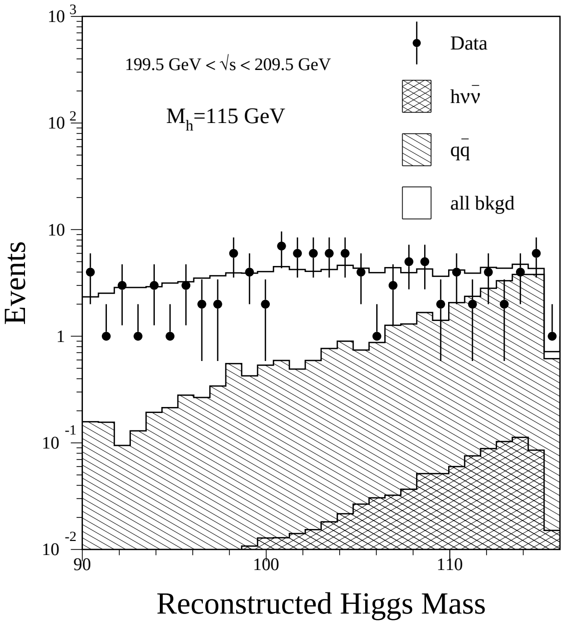

Figure 5.1. Plot of the fitted Higgs mass (m_h^{rec}). The white region respresents the entire Standard Model background, the hatched region represents the $q\bar{q}$ background and the cross-hatched region represents a 115 GeV Higgs mass signal.

5.1.3 The Neural Network

First invented by Cognitive Science researchers, artificial neural networks have been used by scientists in many fields to study cognition and perception [23]. Brain function is modelled with computers in an attempt to understand our thought and learning processes. Scientists have also used neural networks as tools for various tasks in which an element of pattern recognition is involved. Networks can be "trained" to identify patterns or optimize complex functions involving multiple free parameters. The iterative process used can be done very quickly with modern computing capabilities. In the missing energy Higgs search, an artificial neural network [24] is created to aid in the discrimination between signal and background.

The method of back propagation of errors

There are three distinct parts of the neural network: the input layer, the hidden layer(s) and the output layer (see figure 5.2). For simplicity, we'll only discuss the case of one hidden layer here. The input layer contains any number of nodes (x_k) which are connected to each of the nodes of the hidden layer (h_j) and these, in turn, connect to the output nodes (y_i). The strength of the connections between the nodes are called *weights* (w_{ij} and w_{jk}).

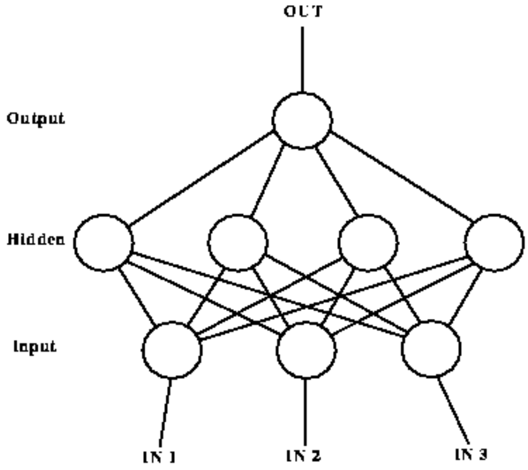

Figure 5.2. Neural network with three input nodes, one output node and one hidden layer containing four nodes.

As each node receives signals, it calculates a weighted sum where its output is determined by a sigmoid function, $g(a, T)$. The variable a is the sum of incoming signals:

$$a_i = \sum_j w_{ij} h_j \tag{5.3}$$

and

$$a_j = \sum_k w_{jk} x_k. \tag{5.4}$$

The variable T in the sigmoid function is called the "temperature". The use of the word "temperature" here is a relic of earlier work [22] that used the physical analogy of annealing. In this process, the lowest energy state of a metal is found by heating it up and then slowly reducing the temperature. In the context of neural networks, the temperature defines the slope of the sigmoid function. For example, the sigmoid function used in this analysis is

$$F(x) = \frac{1}{1 + e^{-x/T}}, \tag{5.5}$$

where T is the temperature. A very large temperature would be too permissive while a low temperature would hinder the network's abiliity to optimize properly.

An error function is defined to be

$$E = \frac{1}{2} \sum_p \sum_i (y_i^{(p)} - t_i^{(p)})^2, \tag{5.6}$$

where t_i is the target output of the ith output node and p is the input/output pattern. When the network is training, it seeks to minimize the error function by changing the weights. The method of gradient descent is used for this. Each change of the weights should correspond to some gradient in the error function:

$$\Delta\omega_{ij} = -\eta \frac{\partial E}{\partial \omega_{ij}} \tag{5.7}$$

and

$$\Delta\omega_{jk} = -\eta \frac{\partial E}{\partial \omega_{jk}} \tag{5.8}$$

where η is the "learning strength parameter" which allows for faster or slower learning, as desired by the creator of the network. By the chain rule,

$$\frac{\partial E}{\partial \omega_{ij}} = \sum_i \frac{\partial E}{\partial y_i} \frac{\partial y_i}{\partial a_i} \frac{\partial a_i}{\partial w_{ij}} = \delta_i g'(a_i/T) h_j \tag{5.9}$$

and

$$\frac{\partial E}{\partial \omega_{jk}} = \sum_i \frac{\partial E}{\partial y_i} \frac{\partial y_i}{\partial a_i} \frac{\partial a_i}{\partial h_j} \frac{\partial h_j}{\partial a_j} \frac{\partial a_j}{\partial w_{jk}} = \sum_i \delta_i \omega_{ij} g'(a_j/T) x_k, \tag{5.10}$$

where $\delta_i = (y_i - t_i)$. So, for gradient descent between the input and hidden nodes,

$$\Delta\omega_{ij} = -\eta \delta_i h_i + \alpha \Delta\omega_{ij}^{old} \tag{5.11}$$

and between the hidden and output nodes,

$$\Delta\omega_{jk} = -\eta \sum_i \omega_{ij} \delta_i g'(a_j/T) x_k + \alpha \Delta\omega_{jk}^{old}, \tag{5.12}$$

where α is called the "momentum term" and is used to dampen oscillations. Note that the weight change between the input and hidden nodes depends on the error calculated between output and target. This is called a back-propagation of error.

Training

Neural network training is done on a set of background and signal Monte Carlo events. During training, the network will find a minimum value for the error function. The number of training cycles necessary for this optimization depends on the number of events used for training. Shown in figure 5.3 is a plot of the error calculation for the training of the 207 GeV network (see table 5.2) as a function of numbers of training cycles. As anticipated, the change in error becomes negligible after a certain number of cycles. For the training used in this analysis, 6 $\times 10^6$ cycles is used.

Running

After the training procedure is completed, a matrix of weights will be available for the "running" segment of the analysis. During running, data as well as Monte Carlo

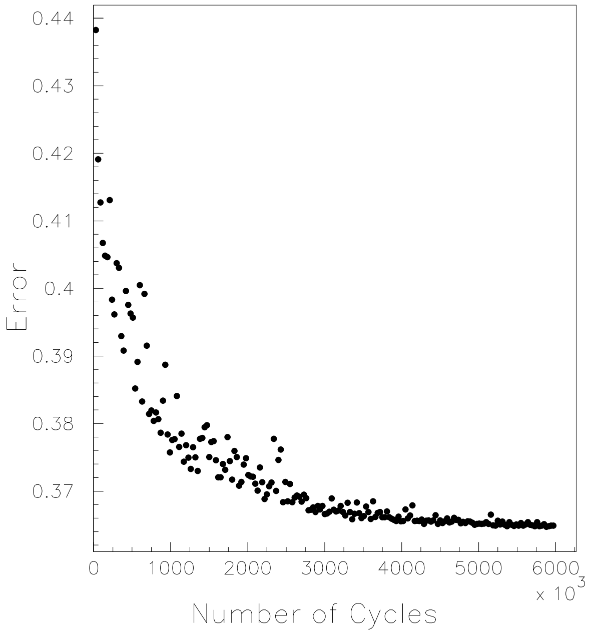

Figure 5.3. Error in the 207 GeV network as a function of the number of training cycles.

background and signal events are given a neural network output value between zero and one, based on their position in the weighting matrix. The range from zero to one corresponds to an event's characteristics being least signal-like to most signal-like. A sign of good neural network performance is the separation between signal and background in the output. The background events should prefer the lower region while the signal events should prefer the higher. In practice, it can be very difficult for a network to make this distinction. A successful network is one that provides a better performing analysis than if hard requirements were used instead.

Neural Network in practice

A neural network is used in the missing energy Higgs analysis to distinguish between signal and background. Eight discriminating variables are used as inputs to the network. As mentioned previously, most of these variables have been selected for their ability to distinguish between signal and $q\bar{q}$ background. These variables, listed below and with distributions shown in figures 5.4 and 5.5, take into account kinematics, event shape and b-tag.

- missing mass

The missing mass is defined as before:

$$M_{missing} = \sqrt{(E_{cm} - E_{vis})^2 - p^2_{missing}}. \tag{5.13}$$

The missing mass distribution for the signal Monte Carlo should peak around 90 GeV because the missing particle is a Z boson. At this stage in the analysis (i.e. after the preselection requirements), the $q\bar{q}$ events left will have missing mass near 110-120 GeV.

- maximum jet width

This variable is defined in following manner:

$$\text{maximum jet width} = max(W_{j1}, W_{j2}) \tag{5.14}$$

where W_{ji} is the width of the *ith* jet. The jet width is caluclated by first finding the average momentum vector of all the constituent particles and then summing the transverse components of each particles momentum vector. The distribution of the maximum width of the jets peaks at small values for Higgs events. In $W^+W^- \to q\bar{q}'l\bar{\nu}_l$ events, the high energy lepton could be included in one of the jets when they are forced into two. This will broaden the measured width of the jet in which the lepton is included. Since this variable looks at the larger of the two jet widths, W^+W^- events in which the lepton is included in a jet will be suppressed.

- b-tag

The b-tag variable takes advantage of the Higgs's predilection for decaying to b-quarks. This variable is described in more detail in section 3.2.12.

- transverse missing momentum/total momentum

  This variable, P_t/P_{total}, is the fraction of the total missing momentum (the ν's) that is transverse to the beam axis. The Higgs signal events peak near 1.0 because the missing momentum vector has no preference to be parallel to the beam axis. Background events coming from $q\bar{q}(\gamma\gamma)$ are most dangerous when the two photons go down the beampipe. These events will have very low transverse missing momentum, so they are suppressed by this variable.

- acoplanarity

  The acoplanarity is a measure of how much the constituents of the event are in the same plane as the beam pipe. A large portion of $q\bar{q}(\gamma\gamma)$ background events have a small acoplanarity because the two photons are usually lost down the beampipe. The conservation of momentum then ensures that the two jets will be in the same plane as the beampipe. Hadronic jets from Higgs events will not be as coplanar as the $q\bar{q}$ background because the neutrinos can go in any direction. The acoplanarity is described, mathematically, in this way: [1]

$$acoplanarity = \frac{\pi - \alpha}{\pi - 2arctan(\frac{m_h^{rec}}{p_{total}})}. \tag{5.15}$$

  A small acoplanarity can also arise if both jets of the event are close to being in the same plane as the beampipe (i.e. back-to-back). This variable is also good at discriminating a $m_h = 115$ GeV Higgs signal from W^+W^- and single-W background because these two background processes will not result in back-to-back jets. Therefore, the acoplanarity distributions of the W^+W^- and single-W backgrounds will peak higher than a $m_h = 115$ GeV signal.

---

[1] The variable α is π minus the angle between the plane containing the two jets and the beam axis.

- sjet

The sjet variable is described in this way:

$$sjet = \frac{2\pi - \beta}{2\pi - 4 \cdot arctan(\frac{m_h^{rec}}{p_{total}})}. \tag{5.16}$$

The β variable is constructed by forcing each event into three jets and summing the angles between them. The maximum of the sum of angles between the vectors is 2π radians. The distribution of high Higgs mass signal events will peak at low values of the sjet variable defined above. Single-W ($qq'e\nu_e$) background events peak at higher values because events with the final state electron associated with one of the jets will be easily forced into three jet events all three "jets" are not neccessarily in the same plane. In these cases, the sum of the angles will be smaller than for three jets lying in the same plane.

- visible mass/reconstructed mass

The fraction of visible mass over the reconstructed Higgs mass gives an idea of how much mass was "added" by the constrained fit. We would expect that a Higgs signal event would have a reconstructed mass very close to that which was calculated by the kinematic fit. This is why the signal distribution of this variable peaks near one. The $q\bar{q}$ background will, in general, have less visible mass than the kinematic fit routine assigns to the jets. The jets should peak near the Z mass but the fit pushes this up higher, as discussed earlier. As promised, the $q\bar{q}$ distribution peak is well separated from the signal peak, making this a good discriminating variable.

- error in the kinematic fit

The error in the kinematic fit is defined by the following equation:

$$Error = \sqrt{\frac{(E_{jet_1} - K_{jet_1})^2}{E_{jet_1}} + \frac{(E_{jet_2} - K_{jet_2})^2}{E_{jet_2}}}, \tag{5.17}$$

where K_{jet_i} is the energy of the *ith* jet as assigned by the kinematic fit routine described in section 5.1.2. A traditional χ^2 is defined like

$$\chi^2 = \sum_{i=1}^{n} \frac{(m_i - f_i)^2}{\sigma_i^2}, \tag{5.18}$$

where m_i is the measured quantity, f_i is the fitted quantity and σ_i is the variance of the measured quantity[2][25]. Since the measurement E_{jet_i} is based primarily on the the calorimeter measurement, for which $\sigma_i \propto \sqrt{E_{jet_i}}$, the error variable above is approximately a rescaled $\sqrt{\chi^2}$ with units of $[\text{energy}]^{\frac{1}{2}}$. Like m_{vis}/m_h^{rec}, this variable helps discriminate against background events whose jet energies after the kinematic fit are far from their measured values. This is especially helpful in suppressing $q\bar{q}(\gamma\gamma)$ events.

Distributions for these neural network input variables are shown in figures 5.4 and 5.5. All of these distributions show good agreement between data and Monte Carlo.

bin name	$\sqrt{s}$ range(GeV)	signal MC(GeV)	background MC(GeV)
202	199.5-203.5	202.0	202.0
205	203.501-205.5	205.1	205.2, 206.0*
207	205.501-207.5	206.6	206.6
208	207.501-209.5	208.2	208.0

Table 5.2. Signal and background Monte Carlo used for neural network training.* The single-W background Monte Carlo used for the 205 GeV network was generated at 206.0 GeV.

Four distinct networks are trained in order to take into account the range of center-of-mass energies. The energy ranges of these networks are shown in table 5.2. From the signal sample, only Higgs-strahlung events generated with m_h = 111-117 GeV (in 1.0 GeV steps) are used in the training. This mass range is used in order to execute a high mass search with a sufficiently large training sample size. In

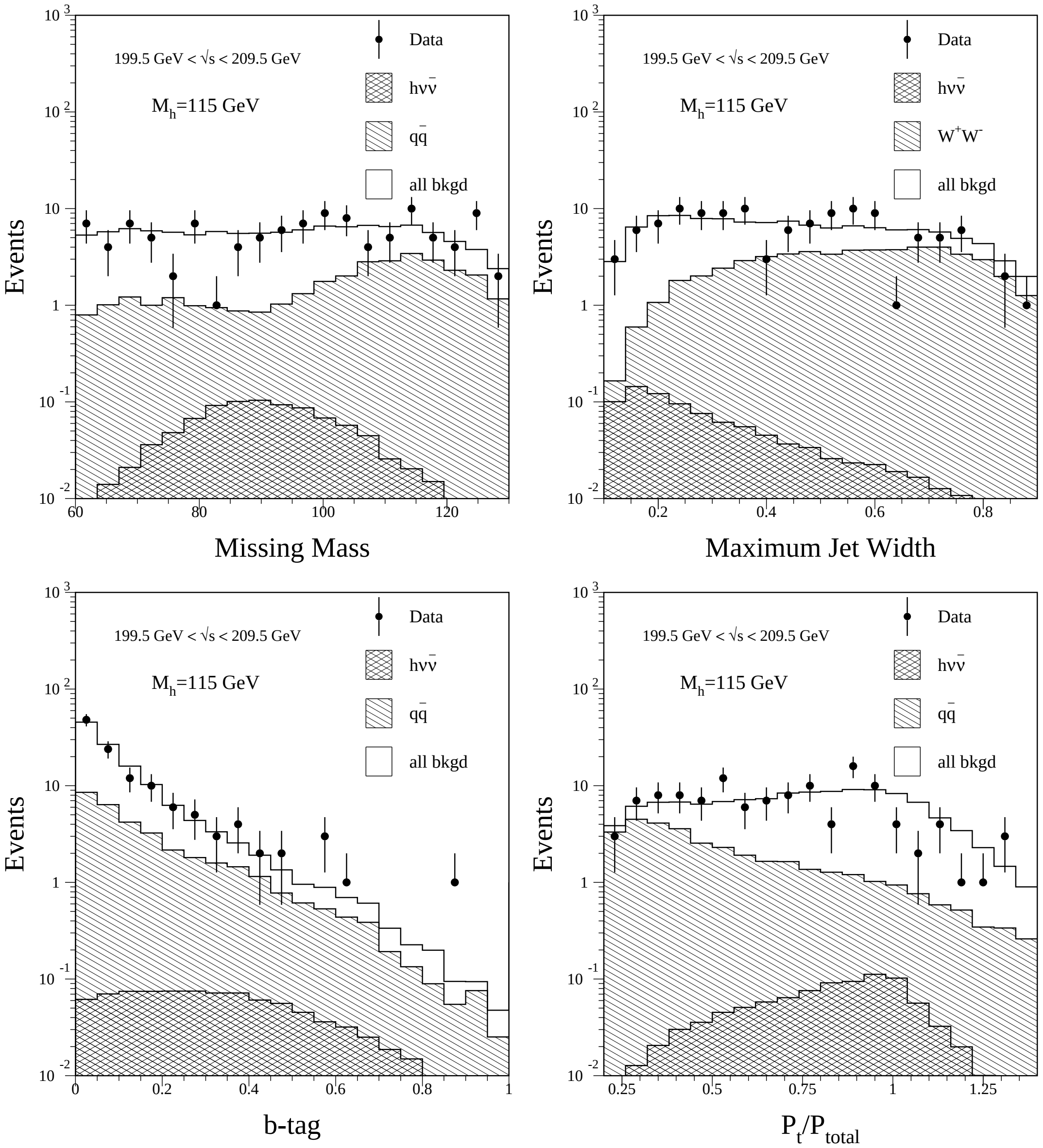

Figure 5.4. Neural network input distributions for missing mass, maximum jet width, b-tag and p_t/p_{total}. A Standard Model background for which each variable is especially discriminating is shown (hatched). In all cases, the signal distribution (cross-hatched) is shown for m_h= 115 GeV.

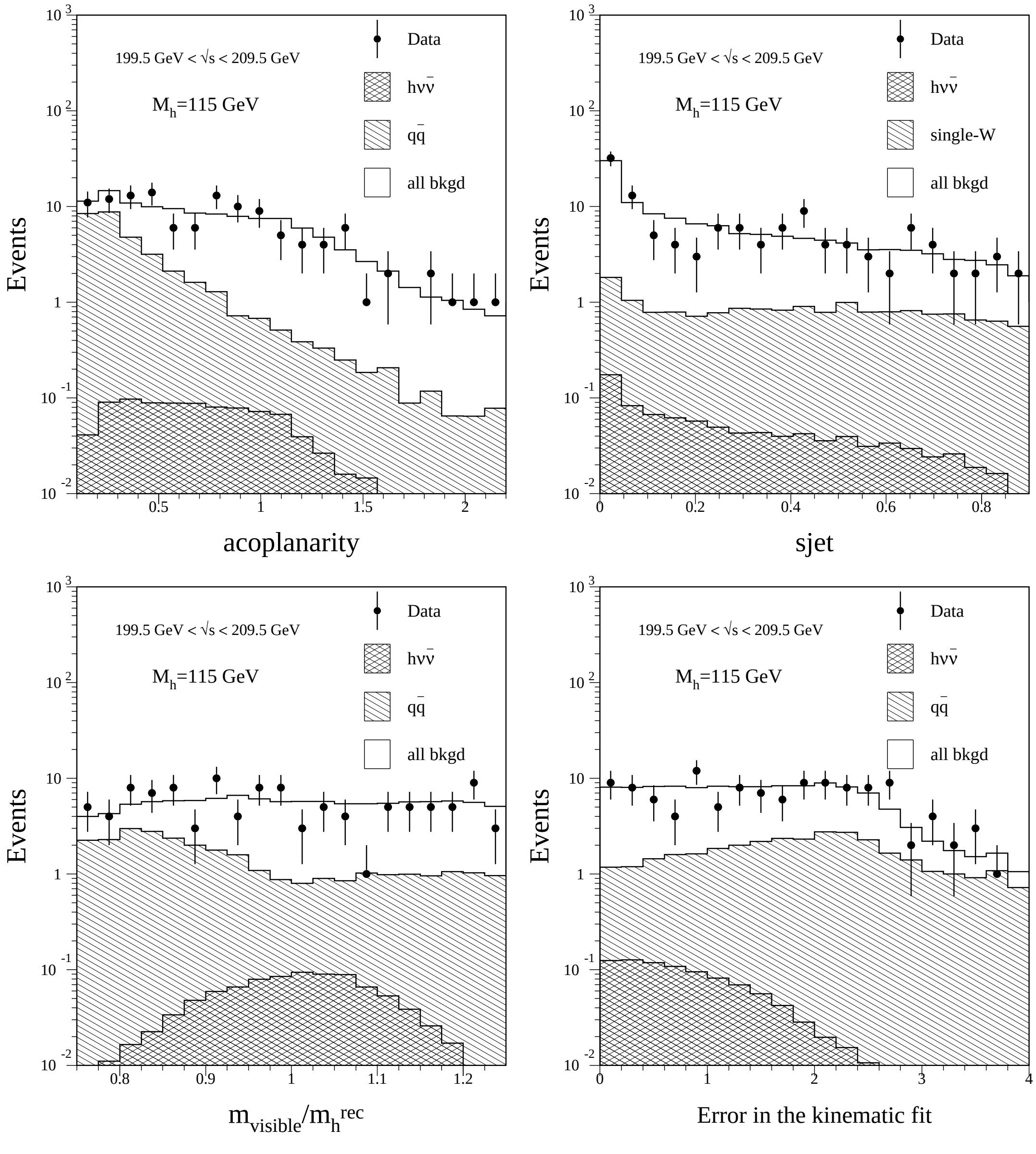

Figure 5.5. Neural network input distributions for acoplanarity, sjet, $\mathrm{m}_{visible}/\mathrm{m}_h^{rec}$ and the error in the kinematic fit. In all cases, the signal distribution (cross-hatched) is shown for m_h= 115 GeV.

the background sample, $q\bar{q}$, W^+W^- and single-W Monte Carlo events are used. The network doesn't train on ZZ because the topology is so similar to that of signal events that the performance would deteriorate. Instead, this background is suppressed by the next step in the analysis procedure (described below). Single-Z background isn't used in the training because so few events pass the preselection cuts. The output of the neural network for the entire E_{CM} range is shown in figure 5.6.

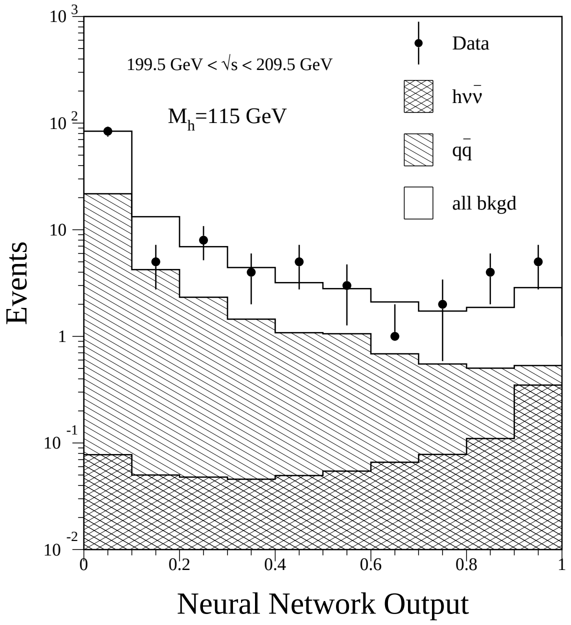

Figure 5.6. Plot of the neural network output (NN_{out}) for the entire range of $\sqrt{s}$.

The data and Monte Carlo show good agreement throughout. Note the different shapes for the signal and $q\bar{q}$ distributions. As expected, the signal peaks near NN_{out} = 1.0 and the $q\bar{q}$ background peaks near NN_{out} = 0.0.

5.1.4 The Final Discriminant

To evaluate the significance of a data event, a final discriminant variable is created by combining the output of the neural network (NN_{out}) and the fitted Higgs mass (m_h^{rec}). The histograms are called probability density functions (PDF). The NN_{out} histogram has a range of 0 to 1 while the m_h^{rec} histogram has a range of 70 to 130 GeV; each contain 100 bins. Each data point has values for NN_{out} and m_h^{rec} that corresponds to a particular bin in the respective PDF. For example, if an event has a $m_h^{rec} =$ 104.5 GeV, it will be located in the 58th bin of the m_h^{rec} histogram. A probability is determined by calculating what fraction of events from each event type lies within this bin. This procedure is done for signal as well as for all five of the backgrounds. Of course, the m_h^{rec} histogram will vary for each Higgs mass under consideration, so a scan must be carried out over many histograms, each representing one Higgs mass hypothesis. For this analysis, the Higgs mass range being investigated is from 70 GeV to 95 GeV in 1.0 GeV steps and from 95 GeV to 120 GeV in 0.1 GeV steps. For the NN_{out} histogram, a similar procedure is done to derive a probability for each event type (5 backgrounds + signal) in each bin. In the case of the NN_{out} variable, each event is then weighted by its respective efficiency times cross section times the collected luminosity to turn the probability into numbers of expected events in each bin. The choice of turning the probability associated with the neural network output instead of the m_h^{rec} probability into numbers of events is arbitrary. It is neccessary, however, to do this for one of them so that the relative cross section weightings are taken into account. The probability from the m_h^{rec} distribution and number of events (calculated using the NN_{out} variable) are combined to find a purity for each event. The purity for an event lying in the *ith* bin of the m_h^{rec} distribution and the *jth* bin of the NN_{out} distribution is defined as

$$Purity = \frac{P_{signal_i} \times N_{signal_j}}{P_{signal_i} \times N_{signal_j} + P_{background_i} \times N_{background_j}} \tag{5.19}$$

where

$$P_{background_i} \times N_{background_j} = P_{q\bar{q}_i} \times N_{q\bar{q}_j} + P_{WW_i} \times N_{WW_j} + P_{ZZ_i} \times N_{ZZ_j} + etc. \tag{5.20}$$

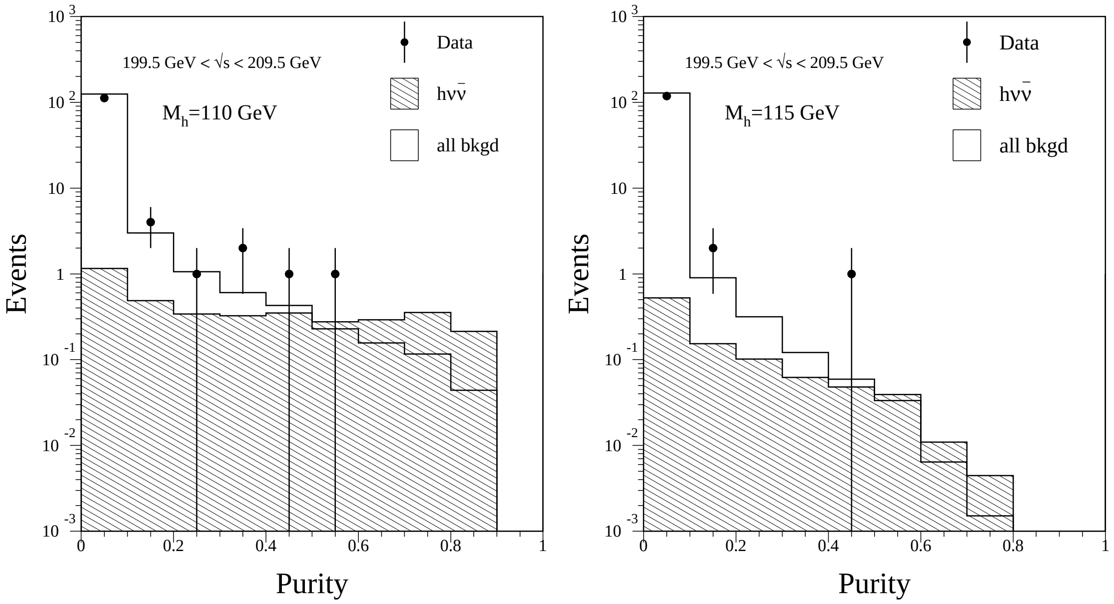

Figure 5.7. Plots of the purity distributions for Higgs mass hypotheses $m_h = 110$ GeV (left) and $m_h = 115$ GeV (right) for the entire $\sqrt{s}$ range (i.e. all of the year 2000 data). The white region represents the entirety of the Standard Model background. The shaded region represents 110 GeV and 115 GeV Higgs signals, respectively.

The purity should have high values for the most signal-like events and low values for the most background-like events. In fact by looking at equation 5.19, it's easy to see that the signal-like and background-like regions will intersect at purity $= 0.5$. We use the purity to determine if there is any indication of signal in the data sample and, if so, how strong this indication is. A distribution of the purity for the total luminosity is shown in figure 5.7.

By the definition of the purity, events with purity greater than 0.5 have a locally binned signal/background ratio greater than one. The larger an event's signal/background ratio is, the better the candidate is. One should note, however, that there is background present throughout the purity distribution, so an event in any bin could be coming from background.

For illustrative purposes, the numbers of expected and observed events for selected benchmark cuts on the purity are shown in tables 5.3 and 5.4 for the $m_h = 110$ GeV and $m_h = 115$ GeV hypotheses, respectively.

$200 \le \sqrt{s} \le 209$ GeV	m_h=110 GeV						N_{data}
	$N_{background}$			N_{signal}			
Purity cut (s/b)	$q\bar{q}$	ZZ	total	HZ	WW	total	
0.05 (0.05)	4.9	2.0	10.7	3.0	0.25	3.3	13
0.1 (0.11)	2.6	1.2	5.6	2.6	0.20	2.8	9
0.2 (0.25)	1.2	0.66	2.6	2.2	0.14	2.3	5
0.4 (0.67)	0.43	0.31	0.98	1.5	0.08	1.6	2

Table 5.3. Numbers of background, signal and data events left after increasing cuts on the purity for the Higgs mass hypothesis $m_h = 110$ GeV. The numbers in parenthesis next to the purity cut is the local signal over background fraction at that purity. The numbers of background events are shown for the $q\bar{q}$, ZZ and the total for all the backgrounds combined ($q\bar{q}+ZZ+W^+W^-+$ etc.). The numbers of signal events are shown for the Higgs-strahlung and WW-fusion production mechanisms and then the total of both.

For $m_h = 110$ GeV, there is a small, statistically weak excess of data that is consistent with the signal plus background hypothesis throughout the purity distribution. In the purity distribution for $m_h = 110$ GeV (the left side of figure 5.7) there is a significant event with a signal over background ratio greater than one. This is a 110.1 GeV candidate that will be discussed in section 5.2.4. In the most significant region (s/b $>$ 0.67), the $q\bar{q}$ background accounts for about 44% of the background and ZZ is responsible for about 32%. Most of the remaining background is from W^+W^- pair production (20% of the total background).

$200 \le \sqrt{s} \le 209$ GeV	m_h=115 GeV						N_{data}
	$N_{background}$			N_{signal}			
Purity cut (s/b)	$q\bar{q}$	ZZ	total	HZ	WW	total	
0.05 (0.05)	1.9	0.7	3.3	0.55	0.14	0.69	5
0.1 (0.11)	0.83	0.34	1.4	0.42	0.09	0.51	3
0.2 (0.25)	0.33	0.14	0.54	0.27	0.04	0.31	1
0.4 (0.67)	0.07	0.03	0.10	0.10	0.008	0.11	1

Table 5.4. Numbers of background, signal and data events left after increasing cuts on the purity for the Higgs mass hypothesis $m_h = 115$ GeV. The numbers in parenthesis next to the purity cut is the local signal over background fraction at that purity. The numbers of background events are shown for the $q\bar{q}$, ZZ and the total for all the backgrounds combined ($q\bar{q}+ZZ+W^+W^-+$ etc.). The numbers of signal events are shown for the Higgs-strahlung and WW-fusion production mechanisms and then the total of both.

For $m_h = 115$ GeV, there is an overall excess of data events that persists throughout the purity distribution. This excess is consistently greater than the signal plus background hypothesis but is most pronounced above s/b = 0.67. In this region, 0.21 events are expected in the m_h = 115 GeV signal plus background hypothesis while one data event is recorded. This event will be more thoroughly investigated in the candidate discussion section (5.2.4). In the most significant (signal-like) region, the $q\bar{q}$ background makes up 70% of the total background while the remaining 30% is due to ZZ production. Note that the WW-fusion Higgs production mechanism accounts for about 7% of the total expected signal. This is due, in part, to the relative minuteness of the WW-fusion cross section (see section 2.1) as well as the fact that the analysis was optimized for Higgs-strahlung production.

5.2 Results of the missing energy Higgs search

5.2.1 The Log Likelihood Ratio

Construction

A good way of determining whether a set of data is more consistent with background than with signal + background is by the construction of a log likelihood ratio. The purity distribution shown in the previous section is binned so it can be treated with Poisson statistics. The probability of observing n_i events in an arbitrary bin (i) that contains some average expected number of signal (S_i) and/or background (B_i) Monte Carlo events is given by,

$$P(n_i, x_i) = \frac{1}{n_i!} x_i^{n_i} e^{-x_i} \tag{5.21}$$

where $x_i = B_i$ or $S_i + B_i$.

The likelihood is defined as the product of all the probabilities for every bin.

$$\mathcal{L} = P(n,x) = \prod_{i=1} \frac{1}{n_i!} x_i^{n_i} e^{-x_i} \tag{5.22}$$

The likelihood ratio ($\mathcal{Q}$) is defined to be the likelihood of signal plus background over that of background-only:

$$\mathcal{Q} = \frac{\mathcal{L}(S+B)}{\mathcal{L}(B)} \tag{5.23}$$

By a little algebra, one can come to an equation for the natural logarithm of $\mathcal{Q}$,

$$ln\mathcal{Q} = -S_{tot} + \sum_i n_i ln(1 + \frac{S_i}{B_i}) \tag{5.24}$$

5.2.2 Missing energy results

The quantity $-2ln\mathcal{Q}$ can be plotted versus the investigated Higgs mass (figure 5.8). The upper dotted line is the background expectation, the lower dotted line is the expectation of signal plus background, and the wiggly line is the observed data. For each mass hypothesis, a large number of background-only experiments is simulated. The variance in $-2ln\mathcal{Q}$ of these experiments is used to find the 1σ and 2σ deviations. The shaded region closest to the background-only line encompasses the area which is less than 1σ away from being background. The wider shaded region indicates 2σ variation. The separation between the signal plus background and the background-only lines reflect the sensitivity of the search. As the two lines diverge, the signal plus background line moves beyond 2σ from the background-only hypothesis. Hence, the

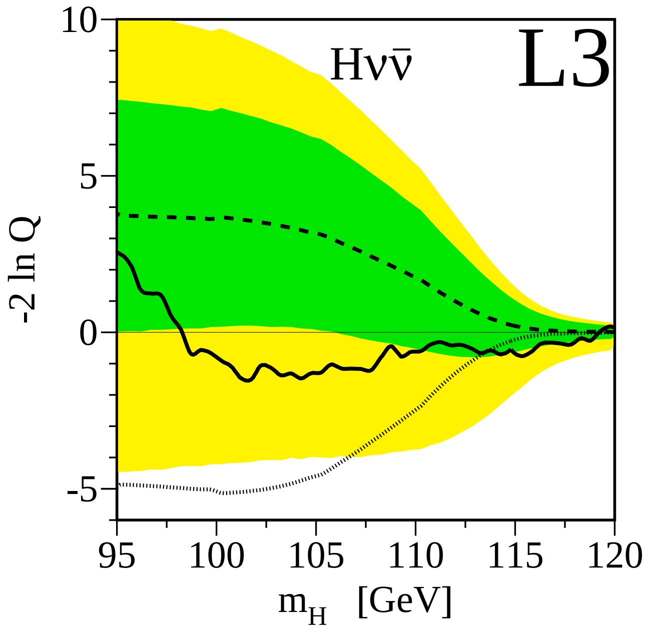

Figure 5.8. Log likelihood curve for the missing energy Higgs search. The upper dotted line represents the expectation for background-only, the lower dotted line represents the expectation for signal + background and the solid, wiggly line represents the observed. The darker shade, closest to the background-only line indicate the region which is within 1σ of the upper dotted line. Likewise, the lighter shaded region represents the region within 2σ of background-only.

analysis becomes better suited to distinguish between the two at lower masses. Note that below $m_h = 100$ GeV, the two lines begin to converge again. This is because the optimization for a high mass search compromises the performance of the analysis at lower masses. Prior to this search, the Higgs mass limit was set at $m_h > 102.6$ GeV with a 95% CL and $m_h > 100$ GeV with $> 99\%$ CL [2] so no signal was expected below this region.

From figure 5.8, one can see that the data is roughly 1σ away from the background-only line at $m_h > 110$ GeV. This excess is mostly due to the 115 GeV and 110.1 GeV candidates discussed below. The deviation below $m_h = 110$ GeV is due to the combined effects of several low mass candidates. Note that the expected signal plus background curve does not exceed 1σ at masses greater than about 113 GeV. This means that one would not expect to see an excess larger than 1σ in this channel even if a high mass (greater than 113 GeV) Higgs signal were actually in the data set.

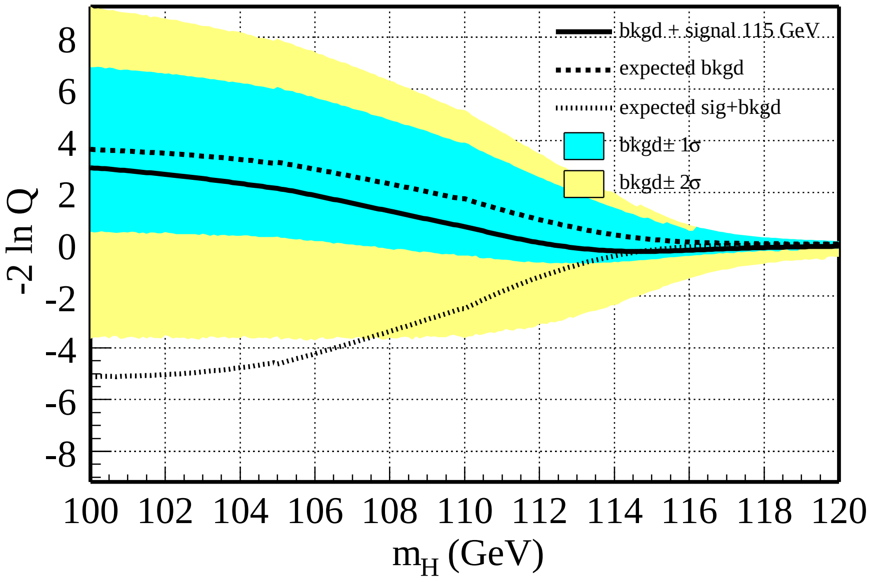

Figure 5.9. Log likelihood distribution of the tail study for the missing energy channel. Signal Monte Carlo generated at a Higgs mass of m_h = 115 GeV is used instead of data. This mock data is shown by the solid line.

5.2.3 Tail study

In order to more fully understand the meaning behind the log likelihood plot, a test is conducted to demonstrate what a Higgs signal should look like. To do this, signal Monte Carlo for a single mass point is used instead of data. The "observed" line will now indicate what we would expect to see from a Higgs signal. It is smoother in figure 5.9 than figure 5.8 because the mock data is allowed to have non-integer numbers of events in each bin. It is called a tail study because it was originally proposed to study the mass resolution of a pure signal plus background observation. The tail study for the missing energy search is shown in figure 5.9 for a Higgs mass of 115 GeV. The width of the signal is not very narrow: an excess is seen for all mass points, never exceeding, however, the 1σ band. This means that even if we were to see the exact signal + background that we would expect for a 115 GeV Higgs, this channel would not be able to claim higher than a 1σ excess. To remedy this, either more luminosity would be needed or the results should be combined with those from the other channels and from other LEP experiments, too.

5.2.4 Candidate discussion

A candidate event for a Higgs signal can be identified in the data sample by constructing a purity from the event's neural network output and reconstructed mass. It was shown in section 5.1.4 that the purity is essentially a 2-dimensional function of these two variables. The local purity of any particular candidate event is therefore based on its position in the NN_{out} and m_h^{rec} distributions. One that scores high in the neural network, will have a good purity in whatever mass region its reconstructed Higgs mass lies. The signal PDF's change as a function of Higgs mass, so by plotting the purity of an event over a range of masses, one should find that it peaks near the nominal reconstructed value and falls off on either side of that value. This can be seen in the candidate evolution plot in figure 5.10 for the three most significant high mass data events in the missing energy channel. Basically the plot shows a variation of the signal to background ratio versus the Higgs mass under investigation.

For the sake of continuity, we begin with the second most significant candidate. This event has a reconstructed Higgs mass of 110.1 GeV and is the most significant candidate in the plot on the left side of figure 5.7. The event came from a collision at $\sqrt{s} = 206.4$ GeV. It has a neural network output of $NN_{out} = 0.88$ and the purity is 0.56 when evaluated in the Higgs mass hypothesis $m_h = 110$ GeV. This purity corresponds to a signal over background ratio of about 1.3.

The most significant high mass candidate seen by the missing energy channel has a reconstructed Higgs mass of 115 GeV. This event occured in a collision taking place at $\sqrt{s} = 206.4$ GeV. The neural network output is $NN_{out} = 0.995$ and the purity is 0.411 for the Higgs mass hypothesis $m_h = 115$ GeV. This purity corresponds to a signal over background ratio of 0.7. From table 5.4, 0.10 Standard Model background events are expected above s/b = 0.67.

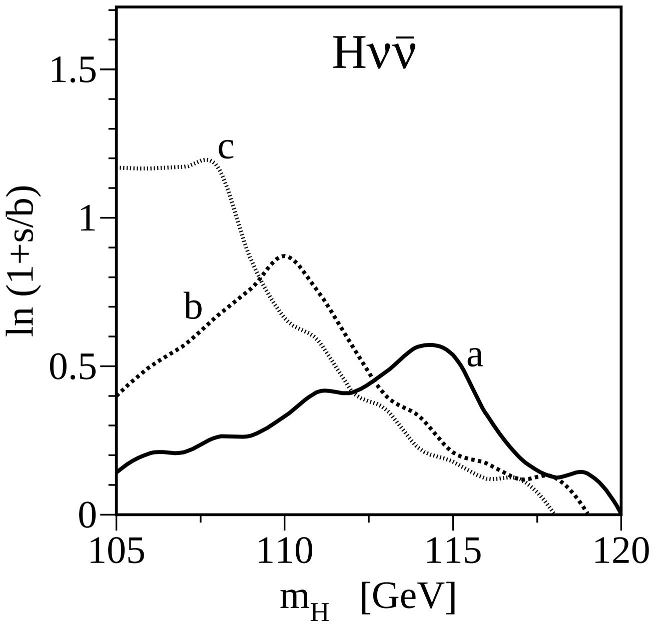

Figure 5.10. Plot of ln(1+s/b) versus Higgs mass for the three most significant high mass Higgs candidates in the missing energy channel. Each curve peaks near the event's nominal m_h^{rec} value: a) m_h^{rec} = 115.0 GeV, b) m_h^{rec} = 110.1 GeV and c) m_h^{rec} = 107.1 GeV. The smooth curves are generated by interpolating between the generated Higgs masses (every 100 MeV).

The candidate has two hadronic jets, almost back to back, as seen in figure 5.11. It should be noted that a fraction of each jet is measured by the SPACAL detectors in the Egap. A study was performed of the energy resolution in this region. Figure 5.12a shows the sum of the measured jet energies for two jet events as a function of the cosine of the thrust angle in the Z calibration data from the year 2000. Figure 5.12b shows the r.m.s. values of figure 5.12a. The arrow in each plot indicates the position of the most significant candidate. From the top plot, we can see that there is no indication of any degradation in the measurement of the energies. From the bottom plot, we can see that the r.m.s. and associated statistical uncertainty of the measurements in this region are not appreciably different from the adjacent regions. We can conclude that the jet resolution is reliable in this region [26]. This is what would be expected, given that the hadronic jets are generally much broader than the region covered by the SPACAL. Only a small portion of each jet actually ends up being measured by the SPACAL.

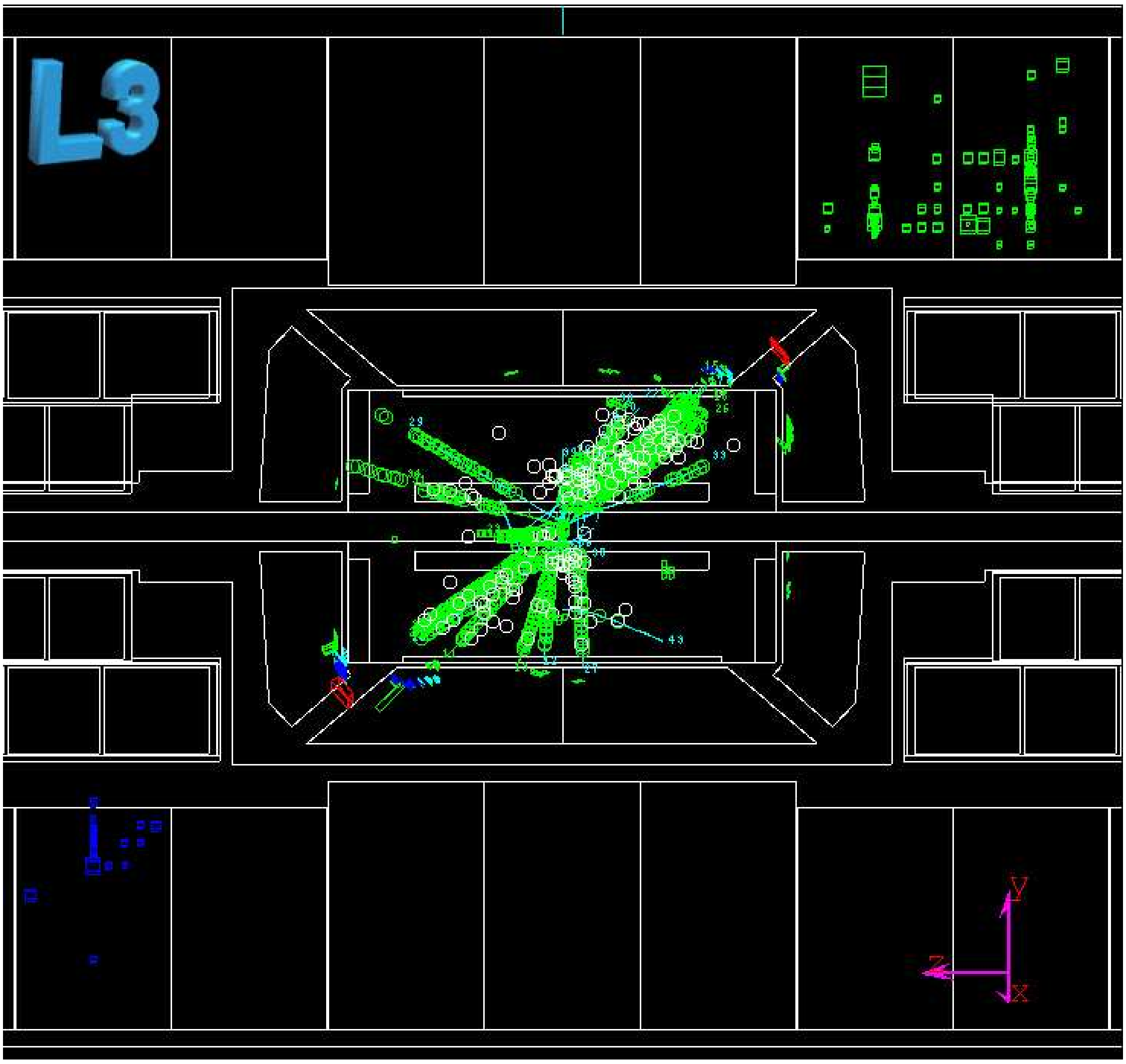

Figure 5.11. In the Y-Z plane: a view of the $h\nu\bar{\nu}$ candidate with m_h^{rec} = 115 GeV. Note the presence of the Egap in portions of the two jets.

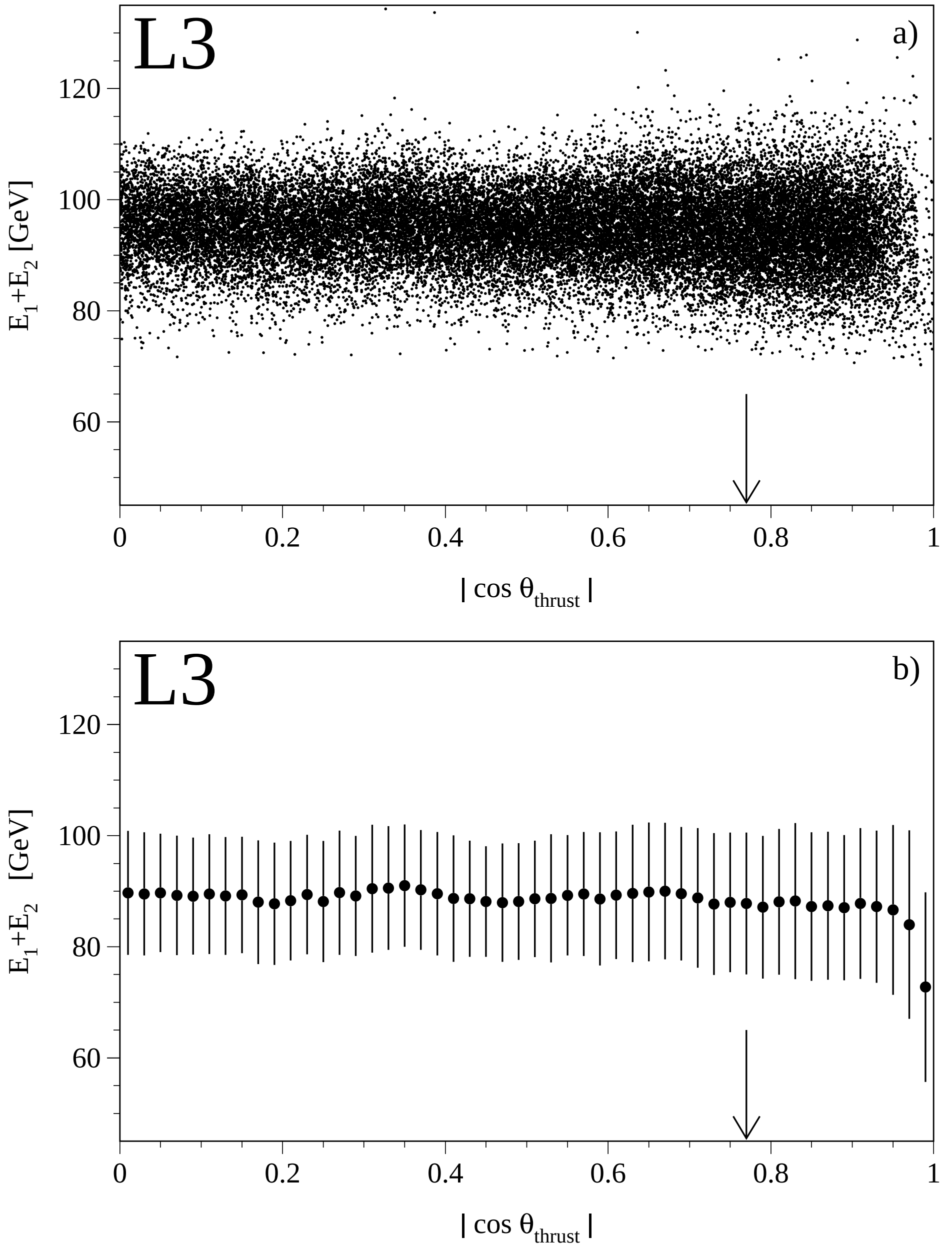

Figure 5.12. Plots of a) the sum of energies of two jet events versus $\cos(\theta_{thrust})$ and b) the average and r.m.s. of a). The arrows indicate indicate the location of the candidate. The Z calibration data from the year 200 run is used.

Historical digression

The Higgs boson candidate event discussed above was recorded by the L3 detector on October 16, 2000 and was identified as a candidate on October 25, 2000. Immediately following, there was an unsuccessful bid to prolong LEP operation beyond its scheduled November 2nd termination date. [2]

The initial characteristics of this event were published in a paper released November 14th [26]. The reconstructed mass of the event was $m_h^{rec} = 114.4$ GeV and the neural network output was $NN_{out} = 0.99995$. The $\sqrt{s}$ was thought to be 206.6 GeV, so at that time the m_h^{rec} distribution peaked closer to the m_h^{rec} of the event, and the candidate had a purity of 0.62, corresponding to a signal over background ratio of 1.6. Between November 2000 and June 2001, a number of changes affected the analysis presented here, including:

- The collected luminosity shifted from 212.5 $\text{pb}^{-1} \rightarrow 217.3\ \text{pb}^{-1}$.
- The LEP center-of-mass energies became more precisely known.
- The data was reprocessed using the final calibration of all the subdetectors, as is done each winter.
- The final evaluation of the detector's behavior throughout the year is carried out and simulated in Monte Carlo events. More Monte Carlo events were produced to reduce statistical unceratinties. The Monte Carlo events were also produced in finer bins of $\sqrt{s}$ (see table 3.1). These new simulations were used to retrain the neural network (without changing any of the input variables).
- New requirements on the photon energy and jet polar angle (see the list of preselection requirements) were introduced. The photon energy cut was implemented to remove a data event with one jet containing a 50 GeV cluster in

---

[2] At this time, the L3 missing energy candidate seemed to give critical support for the Higgs interpretation of three four-jet candidates already reported by the Aleph collaboration. Having two experiments find "golden" candidates in different channels heartened many longtime Higgs hunters.

the ECAL that was identified as a photon (i.e. no associated track). Signal events should not have high energy photons in the final state. This event most likely came from a $q\bar{q}(\gamma)$ background process. The requirement that events must have $E_\gamma < 20$ GeV was implemented as this is the standard used by L3 analyses that wish to suppress these types of events. The performance of the analysis was improved by the inclusion of this requirement. The restriction on the jet polar angle was included when a low significance data event with one jet going partly down the beam pipe was noticed. This kind of event should be excluded from the search because there is no TEC, ECAL or HCAL coverage in the beampipe. Therefore, the jet would most likely be mismeasured. Including this requirement also improved the performance of the analysis.

The most significant of these changes, with respect to the weight of the most significant candidate is the finer $\sqrt{s}$ binning of signal Monte Carlo. Originally, signal Monte Carlo with $\sqrt{s} = 208$ GeV was used in the analysis of the candidate. With this Monte Carlo, the m_h^{rec} distribution for a 114.4 GeV Higgs peaked very close to the candidate's value. Sitting in the highest s/b regions of both the NN_{out} and m_h^{rec}, the event necessarily had a high s/b in the purity distribution and a corresponding high weight (s/b = 1.6). However, with the production of signal Monte Carlo with $\sqrt{s}$ value closer to the true value of the candidate, the m_h^{rec} could no longer peak as close to the candidate's m_h^{rec}. In addition, the candidate's mass also increased slightly and the estimated $\sqrt{s}$ at which it was recorded decreased slightly (206.6 GeV $\rightarrow$ 206.4 GeV). All of these changes conspired to reduce the significance of the candidate. Although the NN_{out} value barely changed (by about 0.5 %), the shift of the m_h^{rec} distribution was enough to lower the weight of the candidate to s/b = 0.7.

5.3 L3 combined results

The results above are combined with the results of the other L3 Standard Model Higgs search channels. The log likelihood curves for the other three channels are shown in figure 5.13 [27], alongside the missing energy channel, for comparison.

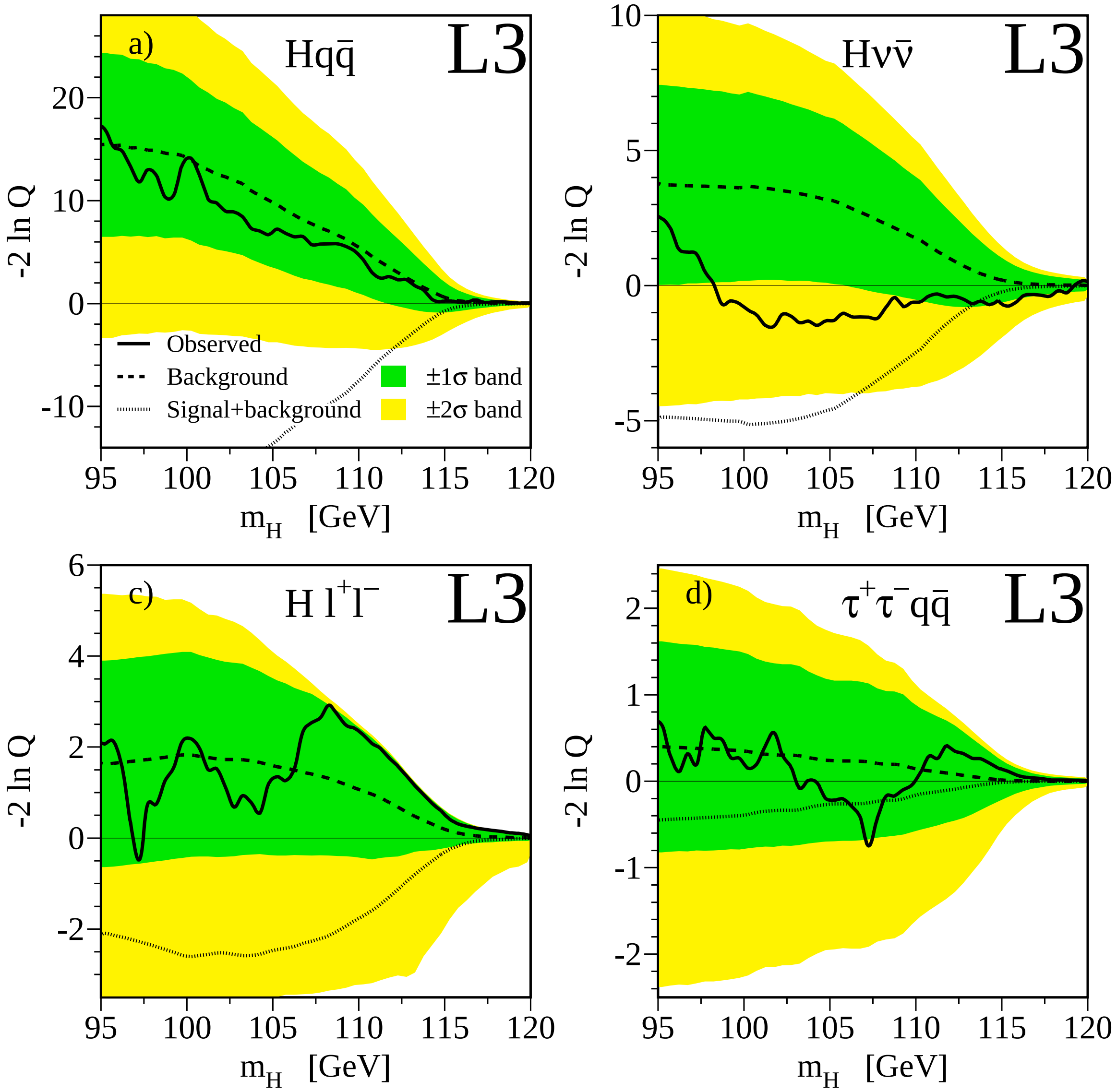

Figure 5.13. The log likelihood curves for a) the 4-jets channel, b) the missing energy channel, c) the lepton channel and d) the tau channel.

The four-jet channel shows good agreement between the observed and the background-only line, never exceeding a 1σ deviation. The lepton channel has a deficit of events

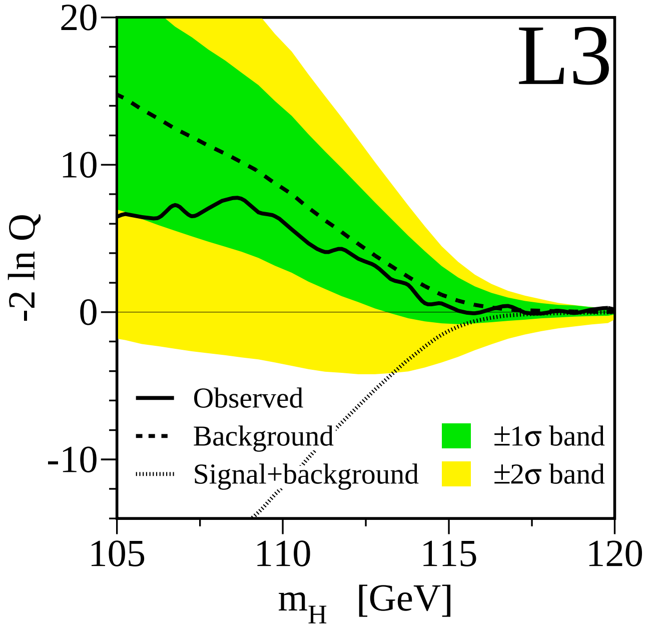

Figure 5.14. Log Likelihood curve for all L3 search channels combined.

for $m_h > 107$ GeV. However, the observation is never further than 1σ away from the background-only line in this region. There are a few lower mass candidates, however, still compatible with the Standard Model background. The tau channel has a slight deficit for $m_h > 110$ GeV, some candidates around $m_h = 107$ GeV, but, still shows an overall agreement with the background-only line.

These channels are combined to produce L3's final results [27]. The log likelihood plot of this combination is shown in figure 5.14. A slight excess of data is seen below $m_h = 116$ GeV, however it does not exceed 1 σ. The combined observation is in very good agreement with the background-only scenario.

5.3.1 Setting confidence limits

Confidence limits can be set using the combined final discriminant histograms for each Higgs mass hypothesis. Following the method in [29], a frequentistic approach is taken. The background confidence limit, CL_b, is found by performing a large number of Monte Carlo experiments (with background MC only), thus generating a distribution of possible outcomes. This distribution is normalized to produce a

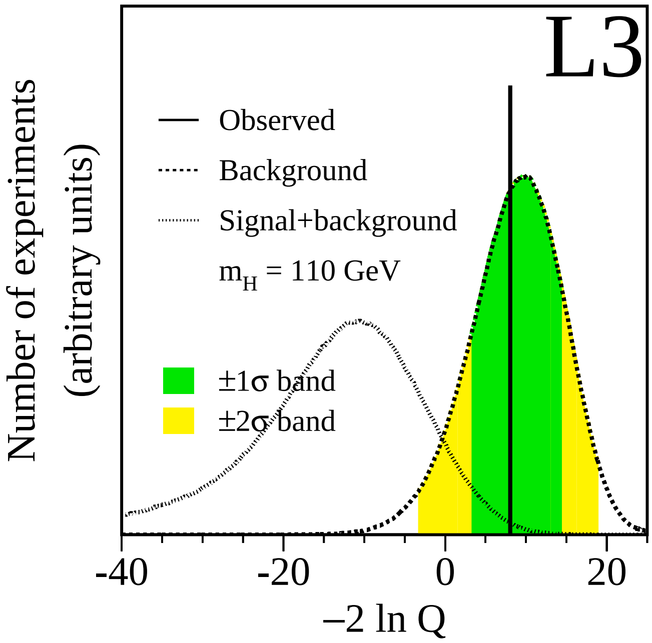

Figure 5.15. Probability density function for $m_h = 110$ GeV. The curve of smaller dots, on the left, is the distribution for signal plus background Monte Carlo. The curve of larger dots, on the right, is the distribution for background-only Monte Carlo. The solid, vertical line shows the position of the data.

probability density function, $\mathcal{F}(\mu)$, where $\mu = -2lnQ$. This is shown in the figure 5.15.

Integrating from negative infinity to the observed value, gives $1 - CL_b$:

$$1 - CL_b = \int_{-\infty}^{obs} \mathcal{F}(\mu) d\mu. \tag{5.25}$$

A plot of 1-CL_b versus Higgs mass hypothesis is shown in figure 5.16. The systematic errors are taken into account when the Monte Carlo experiments are generated (see error estimation discussion below), so they are easily incorporated in the final results. For an experiment in perfect agreement with the Standard Model, we would expect the observed to remain near 1-$CL_b = 0.5$. Any excess would send the observed below this and a deficit of events would correspond to an observed above 0.5. The calculation of the sigma bands is done by the one-sided convention. We accept the Standard Model and look at how far the observed diverges from it in the direction of a Higgs signal (i.e. low $1 - CL_b$). In a gaussian distribution, the variance is well

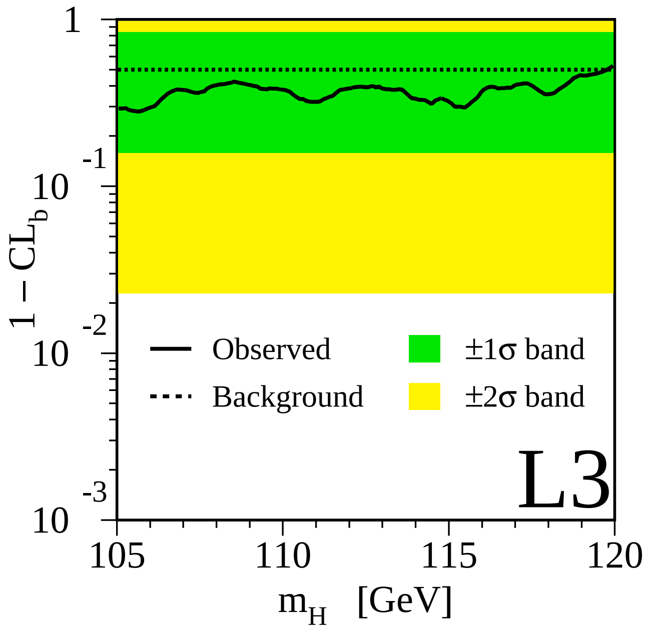

Figure 5.16. Plot of $1-CL_b$ vs. m_h for the L3 combination. Shown confidence bands are calculated with one-sided convention.

defined such that 1σ deviation is at $1 - CL_b = 0.32$, 2σ is at 0.046, and so on [2]. However, if a one-sided convention is used, the CL_b values corresponding to each sigma are half of what they are for the two-sided convention. This is why the 1σ line in figure 5.16 is at $1-CL_b = 0.16$ and the 2σ line is at $1-CL_b = 0.023$. Within this one-sided convention, the data from L3 never goes beyond a 1σ deviation from the background-only line. For $m_h = 115$ GeV, $1 - CL_b = 0.26$.

The signal confidence (CL_s) limit is used to set a lower limit on the mass of the Higgs boson. The CL_s is defined to be

$$CL_s = \frac{CL_{s+b}}{CL_b}, \tag{5.26}$$

where the CL_{s+b} is derived in the same way as the CL_b, using signal plus background Monte Carlo distributions like the one shown in figure 5.15 for $m_h = 110$ GeV. [28]. This conservative definition is adopted to prevent situations in which a serious deficit of data would exclude the Standard Model background-only scenario. All Higgs mass hypotheses below the point at which the CL_s is 0.05 are said to be excluded with

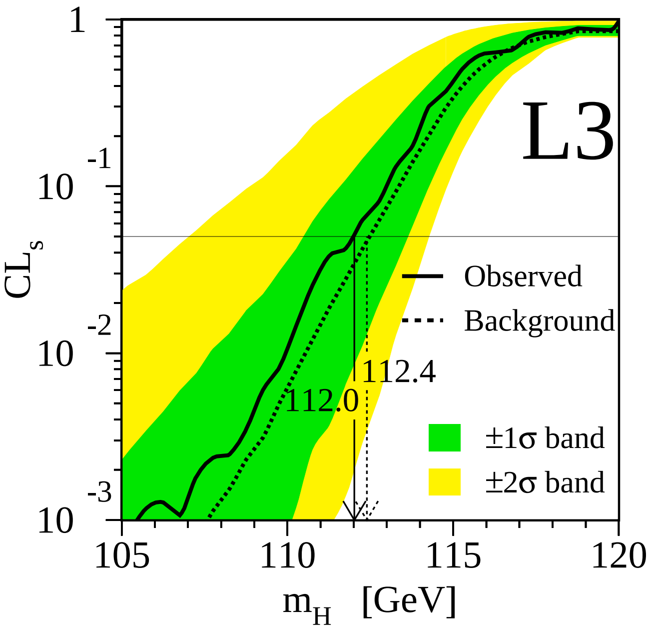

Figure 5.17. The signal confidence (CL_s) as a function of Higgs mass hypothesis (m_h) for the L3 combination. The L3 experiment has an expected limit ($CL_s = 5\%$) at 112.4 GeV and an observed limit at 112.0 GeV.

a 95% confidence. From the Monte Carlo simulations, the L3 experiment expected to exclude Higgs masses below 112.4 GeV. From the data, we exclude Higgs masses below 112.0 GeV (see figure 5.17).

5.3.2 L3 error estimation

No experimental results wold be complete without a proper assessment of the uncertainties involved. Systematic and statistical errors are studied and calculated and the uncertainties derived are taken into account in the results presented in the previous section. Additional studies of ZZ and $q\bar{q}(\gamma\gamma)$ processes are presented in appendix A and appendix B, respectively.

The $q\bar{q}$ background

As the $q\bar{q}$ processes comprise the majority of the high mass Standard Model background for the missing energy channel, it should be well understood. A study is done of possible mismeasurement of full energy events that may, therefore, not be excluded by the preselection cuts. If a full energy $q\bar{q}$ data event (i.e. no initial state radiation) is not accurately measured by the detector, it may pass through the analysis and show up in the final purity plot without being accurately modelled by the Monte Carlo. If this were to happen, an excess of possibly high significance events could slip through and show up as an excess.

To ensure that this has not happened, a test is made. Data and Monte Carlo from the year 2000 Z calibration runs are used to create a model of the jet energy spectrum of full energy $q\bar{q}$ events. The spectrum shows good agreement between data and Monte Carlo. Full energy $q\bar{q}$ Monte Carlo events, defined as events having $E_{jet_1} + E_{jet_2}$ within 17% of E_{CM} at the generator level, in the high energy sample are smeared according to the Z calibration jet energy spectrum. The simulated jet energies are changed according to the spectrum to represent a random jet energy assignment that could occur in a detector mismeasurement. The smeared sample is then compared to the unsmeared sample in the post-preselection distributions. A shift in the smeared Monte Carlo, matching a shift in the data (at low visible energy, for example) would indicate a mismeasurement of full energy $q\bar{q}$ events. The Monte Carlo shift due to the smearing turns out to be very slight and there is no evidence of any mismeasurement of full energy $q\bar{q}$ events.

Systematic errors

Systematic errors on the number of expected background and signal events arise in the predicted production cross sections, detector response, and the $\sqrt{s}$ binning of the data and Monte Carlo [29]. The uncertainty in the LEP center-of-mass energy and in the luminosity measurement are estimated to account for 1% error. There is unncertainty in the number of expected signal events due to imperfect knowledge of M_{top} and α_s [30], interference effects [31] and uncertainty in the quark masses [32]. These will affect the theoretical signal cross sections.

The uncertainty in the detector response is due to uncertainty in subdetector

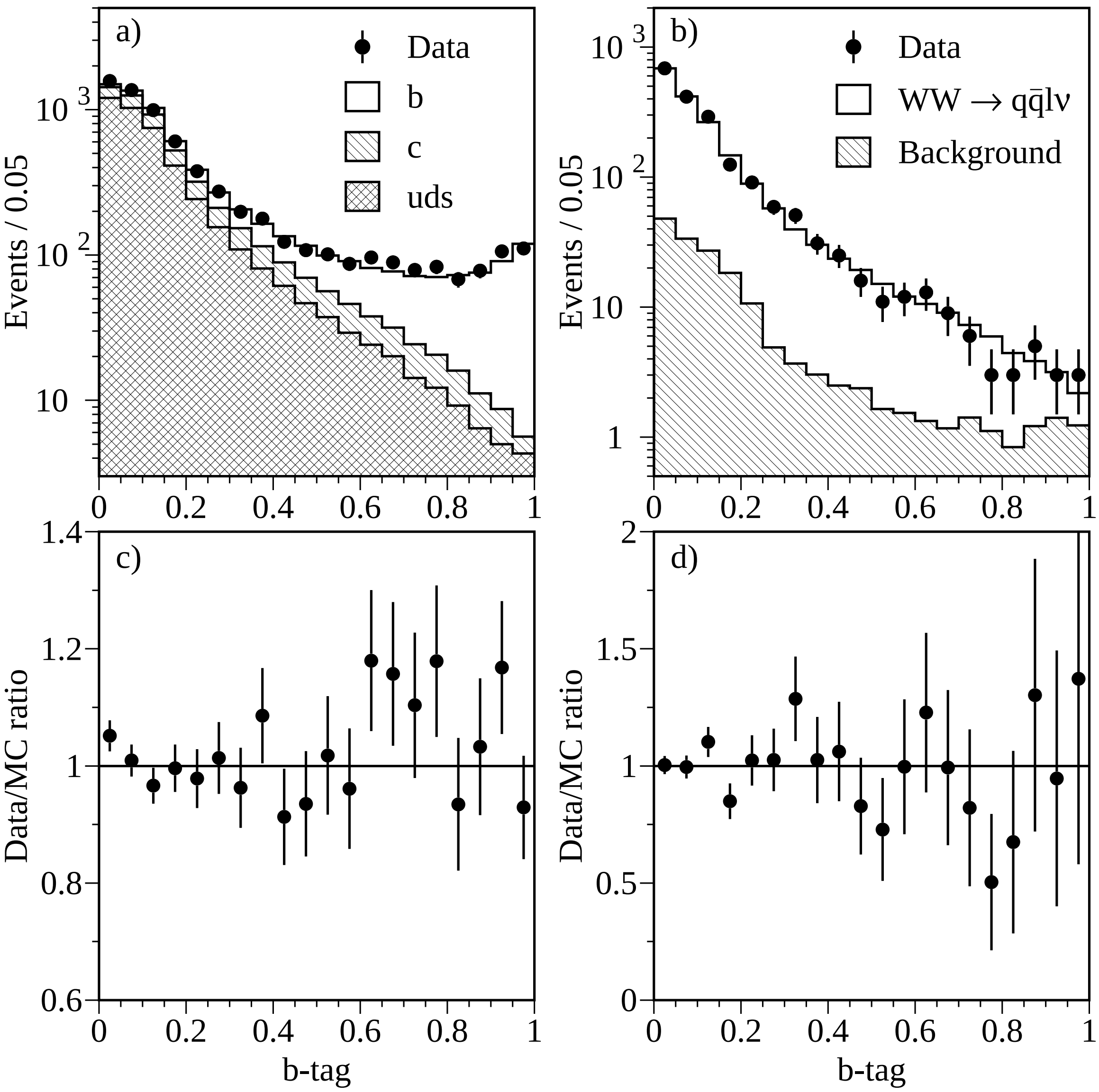

Figure 5.18. Distributions of the jet b-tag for samples of a) $e^+e^- \to q\bar{q}(\gamma)$ and b) $W^+W^- \to q\bar{q}l\bar{\nu}$ events in the high energy data. The ratio of the data and simulated events in each bin are shown in c) and d) for the two processes, respectively.

energy scales, tracking efficiency and b-tagging efficiency. The performance of the b-tag is checked using a sample of $e^+e^- \to q\bar{q}(\gamma)$ events from the high energy data. The efficiency of tagging lighter hadrons is validated with $W^+W^- \to q\bar{q}l\bar{\nu}$ events. Figure 5.18 shows the agreement between data and Monte Carlo for these two processes. Any discrepancy is generally within the statistical uncertainty.

That the luminosity is collected over many center-of-mass energies contributes an additional uncertainty to the number of expected signal events. This uncertainty is estimated by the average variation of the Higgs cross section from the center-of-mass energy at which the Monte Carlo was simulated in each energy bin. For this, the overall uncertainty in the number of signal events is estimated to be from 3% to 6% for m_h close to and beyond the kinematic limit. The largest systematic uncertainty in the background is due to the $q\bar{q}$ events. This is estimated by selecting a sample of $q\bar{q}$ events and comparing the data to the Monte Carlo predictions for various cuts on the acollinearity. The difference in expected and observed cross sections is taken as the uncertainty. The overall systematic uncertainty on the number of background events is estimated to be from 6% to 15% close to and beyond the kinematic limit. However, even a 15% uncertainty in the background events for $m_h = 115$ GeV in the missing energy channel doesn't affect the L3 mass limit. [33]

Statistical errors

A statistical uncertainty is incurred from the finite number of Monte Carlo events. The uncertainties in the numbers of events are estimated to be up to 8% for the background and 4% for the signal. The statistical uncertainty is not correlated bin to bin in the purity distribution and have little effect on the confidence level. This is estimated by introducing fluctuations in the the Monte Carlo trials used to calculate the confidence level.

The uncertainties, statistical and systematic, in the background and signal expectations are included in the calculation of the confidence limits presented above [34].

In order to minimize the effect of the systematic errors on the 95% CL limit, only bins in the final distributions of each search channel with s/b greater than 0.05 are used. The inclusion of the errors reduces the 95% CL by 200 MeV.

5.4 LEP combined results

Since L3 would not be expected to acheive an excess much greater than 1σ in the case of a true 115 GeV Higgs boson, it is necessary to combine its results with those from the other three LEP experiments as a way of increasing the effective luminosity. The preliminary results [35] of those experiments are shown in figure 5.19 along with the L3 final results for comparison. The final results from the rest of the LEP detectors as well as the final combined result is expected to be published during winter 2002.

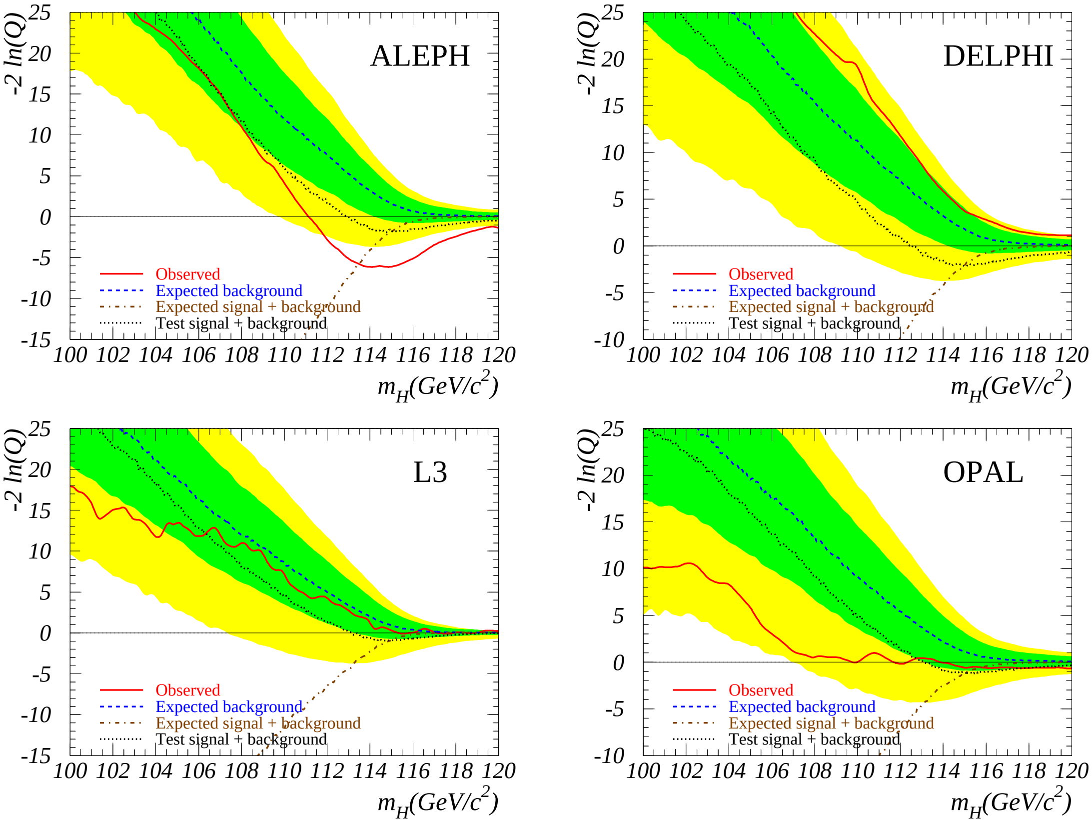

Figure 5.19. Log Likelihood curve for each of the LEP experiments: Aleph, Delphi, L3 and Opal. The tail study curves have also been included for a Higgs mass hypothesis of $m_h = 115$ GeV.

The Aleph experiment has a very significant excess of events in the high mass region. This excess is mostly due to a trio of high mass four-jet candidates. From the tail study line, we can see that the excess is even more pronounced than one would expect from a 115 GeV Higgs. On the opposite end of the spectrum, the Delphi experiment has a general lack of events. Their observation, although within 2σ of the background-only line, is rarely within 1σ. The Opal experiment has an excess of data events with the observation very close to the tail study at Higgs masses above 112 GeV. The combination of all four experiments is shown in figure 5.20.

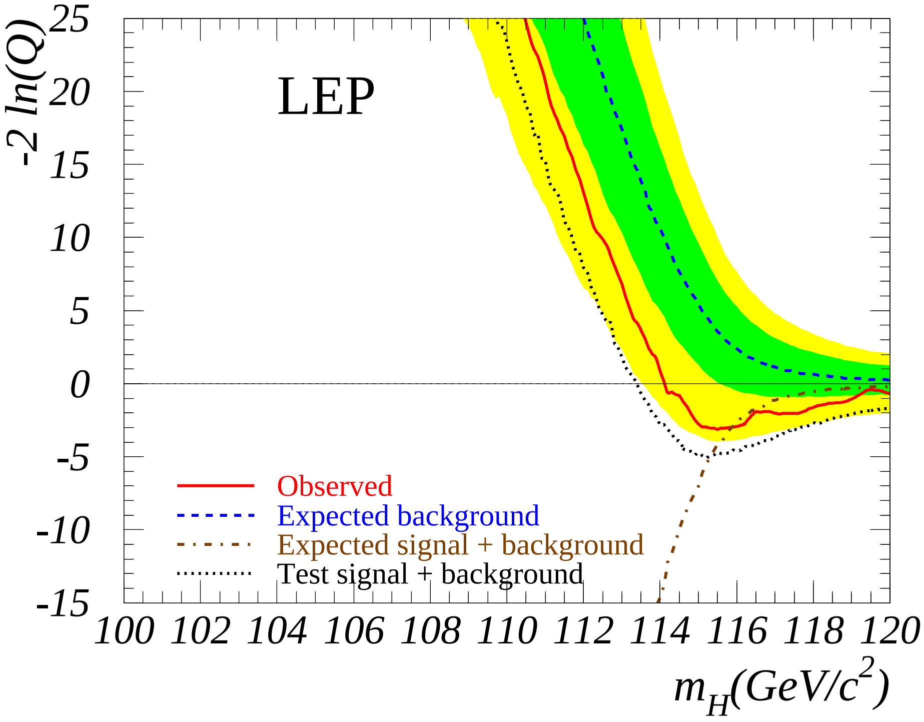

Figure 5.20. The Log Likelihood curve for all four LEP detectors combined.

In the combination, the excess seen by Aleph is somewhat counterbalanced by Delphi's deficit. There is still an overall excess of data events with the largest deviation from the background-only line at $m_h = 115.6$ GeV. The shape of the observed is very similar to that of the tail study, however the data events don't give as large an excess as we'd expect from a pure 115 GeV signal.

As no discovery of the Higgs boson has been made, a lower limit on its mass is set.

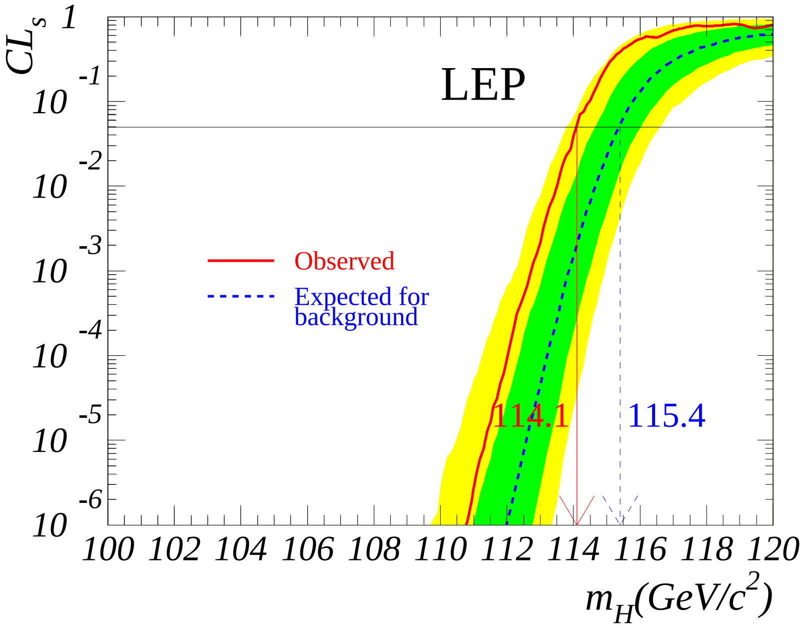

Figure 5.21. Plot of CL_s vs. Higgs mass for the LEP experiments combined.

At the 95% confidence level, the expected limit is $m_h = 115.4$ GeV and the observed limit is 114.1 GeV.

Whether this plot shows a true Higgs signal or an overfluctuation of Standard Model background is a speculative question that cannot be answered with the current set of data (see section 5.5). LEP would have needed about 200 pb^{-1} of more data at $\sqrt{s} > 207$ (approximately one year of additional data) to be able to achieve the 5σ excess needed to claim a discovery.[36]

5.5 Future prospects

The LEP collider had its final collision on November 2, 2000. The results presented in this work represent the end of an era of Higgs searches in electron-positron collisions. There are proposals for higher-energy linear e^+e^- colliders, but these are unlikely to be built soon. The task of Higgs hunting is now in the domain of hadron colliders.

At this moment, Fermi National Accelerator Laboratory (Fermilab) is beginning Run 2 of its Tevatron $p\bar{p}$ collider. The center-of-mass energy of these collisions will be about 2 TeV. Although this is an order of magnitude higher than was achieved at LEP2, the Higgs discovery potential is muddled by the complexity of hadron collisions. When a proton and antiproton "collide", it is really the constituent quarks that are interacting with each other. The energy of an individual quark participating in a given collision is typically less than that of the baryon and unknown *a priori*, so the analysis techniques will have to be different than those used at lepton colliders. The main production mechanisms will be gluon-gluon fusion ($gg \to h$), WW/ZZ fusion, associated tt production ($gg \to tth$) and associated Wh/Zh production. The main search channels will be in $h \to b\bar{b}$, WW^*, ZZ^* and $\gamma\gamma$.

The Tevatron collaborations, CDF and D0, believe that they could exclude with 95% CL up to $m_h \sim 115$ GeV with 2 fb^{-1} of luminosity and up to $m_h \sim 180$ with 17 fb^{-1} [37]. They also state that with the latter amount of integrated luminosty, it would be possible to have a 3σ observation up to ~ 125 GeV and between 150-175 GeV or even a 5σ discovery up to $m_h \sim 110$ GeV. The years by which this much luminosity could be achieved are optimistically given to be around 2004 for 2 fb^{-1} and 2007 for 17 fb^{-1}.

In the abandoned LEP tunnel, a new accelerator is being erected. The Large Hadron Collider (LHC) is scheduled to begin operations around 10 TeV in 2006. Like the Tevatron, the LHC will be using hadronic collisions but with two protons instead of one proton and one antiproton. Antiprotons are more difficult than protons to extract, so not only will the LHC will be able to achieve a much higher energy, but it will also have more luminosity (the larger luminosity is partly due to the higher energy). The LHC collaboration believes that they will be able to record 10 fb^{-1} of data in the first year of running [38]. With this much data, at an order of magnitude larger energy than at the Tevatron, a 5σ discovery up to $m_h \sim 180$ GeV could be made within the first year of data collection.

The inconclusive results of LEP await further experimentation to put to rest the lingering question of whether the first indications of the Higgs boson have already been seen. The race is on between the Tevatron and LHC machines to be the first to end the debate or perhaps even discover the Higgs at some higher mass. The particle physics community eagerly awaits those results.

APPENDICES

APPENDIX A

Study of ZZ production

A.1 Introduction

Studies were conducted of Z boson pair production at center-of-mass energies from 183 GeV to 209 GeV [39]. The results presented here are considered preliminary, with final results to be published in winter 2002. Investigating this process allows us to probe the neutral gauge boson sector of electroweak interactions in the Standard Model. This analysis is presented here because Z pair production constitutes a significant irreducible background to the search for the Standard Model Higgs boson.

The threshold for Z boson pair production was established at $\sqrt{s} = 183$ GeV [40] in 1997, with more data being taken at 189 GeV, 192-202 GeV and up to 209 GeV in 1998, 1999, and 2000, respectively. Special attention is paid here to the data taken in the year 2000, as it corresponds to the data presented in the main body of this work. The ZZ cross section was measured and final states containing b-quarks were studied, as they are most relevant to the Higgs search.

Although the Author was responsible for only the ZZ $\rightarrow q\bar{q}\nu\bar{\nu}$ channel, all analysis channels are presented here for completeness.

A.2 Data and Monte Carlo samples

The data studied was collected by the L3 detector in the year 2000 at center-of-mass energies between 200 GeV and 209 GeV. A total integrated luminosity of 217.8 pb^{-1} was used. The data are grouped into two subsamples: above and below 205.5 GeV (see table A.1).

$\sqrt{s}$ (GeV)	luminosity (pb^{-1})	mean center-of-mass (GeV)
below 205.5	77.8	205.1
above 205.5	140.0	206.8
total	217.8	206.2

Table A.1. Luminosity binning for data taken in the year 2000.

The EXCALIBUR [13] Monte Carlo program was used to generate both signal and background neutral-current four-fermion events. Fermion-pair background was simulated with the KK2f [11] ($e^+e^- \to q\bar{q}(\gamma)$), KORALZ [17] ($e^+e^- \to \mu^+\mu^-(\gamma)$ and $e^+e^- \to \tau^+\tau^-(\gamma)$) and BHWIDE [18] ($e^+e^- \to e^+e^-(\gamma)$) Monte Carlo generators. The background from charged-current four-fermion prcesses was also modelled with EXCALIBUR for single-W and W-pair production. Other processes are described by PHOJET [14] ($e^+e^- \to e^+e^-q\bar{q}$) and DIAG36 [19] ($e^+e^- \to e^+e^-l^+l^-$).

The L3 detector response is simulated using the GEANT [15] program, which takes into account the effects of multiple scattering, energy loss and showering inside the detector. Time dependent detector inefficiencies, monitored throughout the data taking, are simulated as well. The GHEISHA [16] program is used to simulate hadronic interactions within the detector.

The ZZ signal definition differs from channel to channel and is made by kinematic requirements at the generator level of the Monte Carlo. For all channels, the invariant mass of both of the fermion pairs (from each Z) must be between 70 GeV and 105 GeV. Although this is the only signal criterion for the $q\bar{q}\nu\bar{\nu}$ channel, additional requirements are needed for the others. The expected cross sections are computed using the EXCALIBUR Monte Carlo sample with the signal definition imposed. For all the channels combined, the cross sections for the two aforementioned center-of-mass ranges with mean energies of 205.1 GeV and 206.8 GeV are expected to be 1.07 pb and 1.08 pb, respectively. For events whose final states include at least one b-quark pair, the cross section is expected to be 0.30 pb for the entire luminosity range combined.

A.3 The decay channels

The $q\bar{q}q'\bar{q}'$ channel

The events for the ZZ four jet channel are selected to be have high particle multiplicity and a visible energy between $0.6\sqrt{s}$ and $1.4\sqrt{s}$, parallel and perpendicular energy imbalances below $0.3\sqrt{s}$ and no identified lepton or photon with energy above 65 GeV. After being forced to four jets, a constrained fit is employed which rescales the jets to balance momentum while imposing energy conservation. This will reduce the dependence on the calorimeter energy scale.

The main backgrounds after the above selection are from QCD processes and W-pair production. Two artificial neural networks are created in series to reduce these two backgrounds, respectively. Events falling in the high background/low signal regions of the distributions of the network outputs are removed before calculating the ZZ cross section.

The $q\bar{q}\nu\bar{\nu}$ channel

The selection criteria for the $q\bar{q}\nu\bar{\nu}$ channel is somewhat similar to that of the missing energy Higgs search. The topology of the final state is two jets with a large amount of missing energy. In order to rid the data sample of leptonic two-fermion final states and two-photon interactions, events are selected with particle high multiplicity and an invariant mass greater than 50 GeV. Hadronic events from $q\bar{q}(\gamma)$ and W-pair production are reduced by an upper limit of 30 GeV on the invariant mass and setting the minimum allowable mass recoiling against the hadronic system to be 50 GeV. Single-W events as well as semi-leptonic WW decays are targetted with a cut on electrons or muons with energies above 20 GeV. Because of the unbalanced missing energy signature of this channel, the transverse missing momentum is required to be above 5 GeV, the energy deposited in the forward calorimeters must be below 10 GeV and the missing momentum vector cannot be within 16^o of the beam axis. Also, the energy in a 25^o cone around the missing energy vector must not exceed 30 GeV. After these selection requirements, 407 events remain in the data sample, while from the Monte Carlo we expect 339±18 background events and 45±7 signal ($q\bar{q}\nu\bar{\nu}$) events.

An artificial neural network is then employed to further flush out the signal Z-pair events. The machinery of this network is exactly the same as the one used for the missing energy Higgs search. Different variables, however, are employed as inputs to the network. These variables include (among others), an event shape variable to discriminate between two and three jet events, the sum of invariant and missing masses, the masses of the forced two jets, the constrained mass of the hadronic system and the acoplanarity of the two jets. The output of each neural network ($\sqrt{s} < 205.5$ GeV and $\sqrt{s} > 205.5$ GeV) is shown in figure A.1.

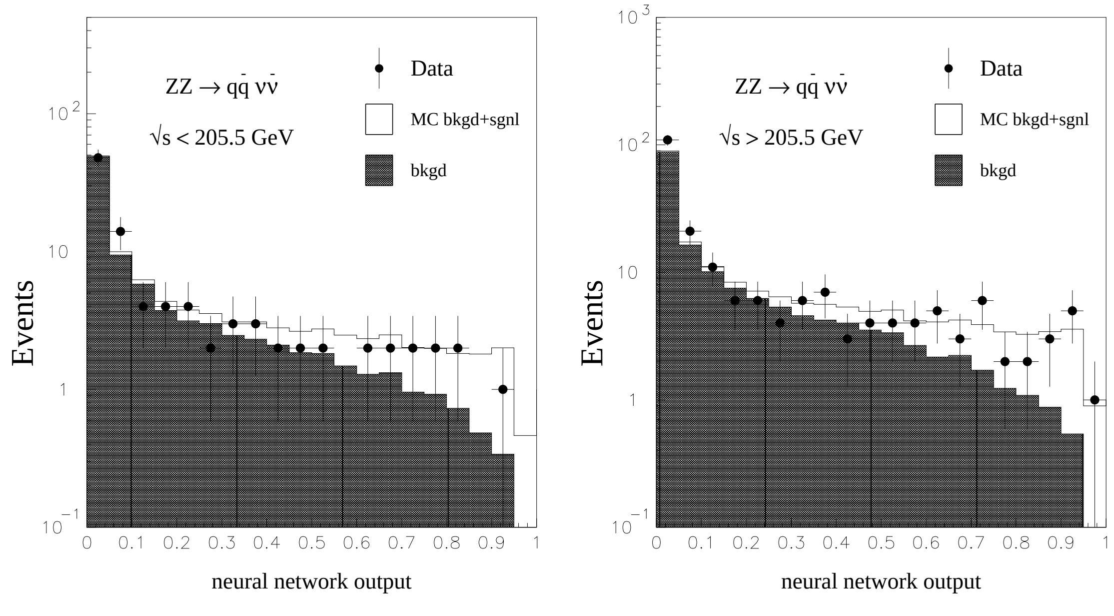

Figure A.1. Neural network outputs for $\sqrt{s} < 205.5$ GeV and $\sqrt{s} > 205.5$ GeV.

A total of 48 data events survive the selection as well as a benchmark cut of 0.5 on the output of the neural network. From the Monte Carlo, we expect 30.8 signal events and 25.4 background events with a signal efficiency of 47%. Table A.2 shows this broken up into the two center-of-mass ranges.

$\sqrt{s}$ (GeV)	Data	Signal MC	Background MC	Signal efficiency
below 205.5	13	10.8	9.4	47%
above 205.5	35	20.0	16.0	47%
total	48	30.8	25.4	47%

Table A.2. Data, signal and background events selected by the $q\bar{q}\nu\bar{\nu}$ analysis. A minimum requirement of 0.5 is made on the output of the neural network.

The cross section for each ZZ final state is determined with a binned maximum likelihood fit using each channel's most significant variable. For the missing energy channel, the neural network output is used. Shown in table A.3 is the observed cross section compared with the one theoretically predicted from the Standard Model.

$\sqrt{s}$ (GeV)	$\sigma_{observed}(pb)$	$\sigma_{theory}(pb)$
205.1	$0.10\ ^{+0.10}_{-0.08} \pm 0.008$	0.30
206.8	$0.29\ ^{+0.09}_{-0.08} \pm 0.022$	0.30

Table A.3. Measured and predicted cross sections for the $q\bar{q}\nu\bar{\nu}$ channel.

The first uncertainty quoted is statistical and the second is systematic. The latter takes into account the uncertainty in the background cross sections, the energy scale of the detector, the jet resolution, the charged track multiplicity and the b-tag. A detailed description of the systematic error estimation can be found in reference [42].

The $q\bar{q}l^+l^-$ channel

A different selection is dedicated to each of the final states, $l = e, \mu$ or τ. A common preselection is applied, requiring a pair of leptons in high multiplicity events with visible energy and effective center-of-mass energy ($\sqrt{s'}$) above $0.5\sqrt{s}$ and $0.6\sqrt{s}$, respectively. $\sqrt{s'}$ is the energy at which the e^+e^- interaction takes place after a possible initial state radiation of photons. It is calculated by taking into account photons observed in the detector as well as those collinear with the beam axis, inferred from the kinematics of the observed particles in the event [41]. For the selection of the electron final state, at least one electron is required to have a matched track. For the muon final state selection, no more than one MIP (minimum ionizing particle) is allowed. The tau selection uses both particle-based and jet-based techniques. The former attempts to identify tau pairs while the latter constrains the event to four-jets and then picks out those with two of the jets having less than four tracks with one of them identified as a tau. Further cuts are performed on each final state to reduce the SM background. In addition, cross efficiencies between the channels are calculated.

The $l^+l^-\nu\bar{\nu}$ channel

Selecting events with a pair of identified leptons is the first criterion of this channel. Tracks are not required for electron identification and MIP's are excluded in the muon identification. The lepton pair must have an invariant mass and recoil mass between 80 GeV and 100 GeV. Further cuts are employed to reduce QCD and four-fermion backgrounds. After these cuts, no contribution from ZZ $\rightarrow \tau^+\tau^-\nu\bar{\nu}$ is expected. The most discriminating variable at the end of the selection process is the sum of the invariant mass of the lepton pair and the recoil mass.

The $l^+l^-l'^+l'^-$ channel

The selection in this channel begins with four loosely identified leptons in low-multiplicity events and then proceeds with kinematic constraints. The energy of the most energetic electromagnetic cluster, the acoplanarity and the acollinearity of the event are used to reject Bhabha and radiative fermion pair-production backgrounds. The most discriminating variable at the end of the selection process is the sum of the invariant mass of the lepton pair and the recoil mass.

A.4 Combined results

After the selections described above, the following results (table A.4) for the total integrated luminosity are found for each final state. The $q\bar{q}q'\bar{q}'$ and $q\bar{q}\nu\bar{\nu}$ entries are reported with a selection requirement of 0.2 and 0.5 on the neural network outputs, respectively.

Final state	Data	Signal MC	Background MC	Efficiency
$q\bar{q}q'\bar{q}'$	604	73.7	512.5	68%
$q\bar{q}\nu\bar{\nu}$	48	30.8	25.4	47%
$q\bar{q}l^+l^-$	31	18.4	6.4	55%
$l^+l^-\nu\bar{\nu}$	6	2.0	1.7	22%
$l^+l^-l'^+l'^-$	2	1.3	1.3	41%

Table A.4. Data, signal and background Monte Carlo events selected by each analysis and their respective efficiencies for all center-of-mass energies combined. The $q\bar{q}q'\bar{q}'$ and $q\bar{q}\nu\bar{\nu}$ entries are reported with a selection requirement of 0.2 and 0.5 on the neural network outputs, respectively.

The results from all the channels are combined assuming their Standard Model predicted relative weights. The measured ZZ cross sections are given in table A.5.

$\sqrt{s}$ (GeV)	$\sigma_{observed}(pb)$	$\sigma_{theory}(pb)$
205.1	$0.86^{+0.23}_{-0.21} \pm 0.07$	1.07
206.8	$1.21^{+0.19}_{-0.17} \pm 0.10$	1.08

Table A.5. Measured and predicted cross sections for all ZZ channels combined.

Again, the first uncertainty is statistical and the second is systematic. Both energy bins show good agreement between the theoretical cross section and the one measured.

A.5 ZZ→ $b\bar{b}$X

A study is done of the b-quark content of Z-pair production final states. This measurement gives us an indication of the detector's capability to resolve heavy quarks. Since most of the Higgs searches include a b-quark pair, this is a very important test. The investigation proceeds for the $q\bar{q}\nu\bar{\nu}$ and $q\bar{q}l^+l^-$ channels by combining, respectively, their most discriminating variables with the b-tag variable described in the main body of this work. The $q\bar{q}q'\bar{q}'$ channel already includes b-tag in the construction of its neural network so it need not be combined again. Because of the low rate, the ZZ → $b\bar{b}$X process is studied with all the luminosity together with the average center-of-mass energy equal 206.2 GeV. The Standard Model prediction for the cross section is 0.30 pb while the measured result is:

$$\sigma_{ZZ\to b\bar{b}X}(206.2 \text{ GeV}) = 0.23 \pm 0.09 \pm 0.02 \text{ pb},$$

The first uncertainty quoted is statistical and the second is systematic. The measured $b\bar{b}$X cross section is in good agreement with the theoretical value. This implies that L3 is well suited to perform a search in which a Higgs boson decays to b-quarks. Shown in figure A.2 is the comparison of the measured ZZ cross section with the one predicted by the Standard Model for the range of center-of-mass energies for which the study has been done at L3. Also shown is the same comparison for the ZZ → $b\bar{b}$X cross section.

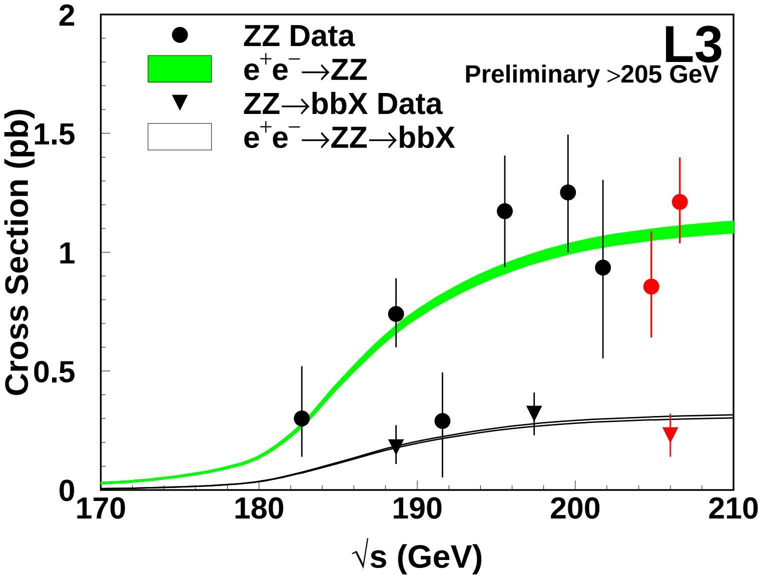

Figure A.2. Comparison of measured and predicted cross section for ZZ pair-production and ZZ→ $b\bar{b}$X.

APPENDIX B

Study of $q\bar{q}(\gamma\gamma)$ events

B.1 Introduction

A study is performed of double radiative return to the Z ($e^+e^- \rightarrow Z\gamma\gamma \rightarrow q\bar{q}(\gamma\gamma)$) events at center-of-mass energies from 200 to 209 GeV. In this process, photons are emitted from both the electron and positron, bringing the effective center-of-mass energy down to around the mass of the Z boson (see figure B.1). The Z boson subsequently decays into a quark, anti-quark pair which then hadronize into particle jets. Therefore, the final state has, nominally, two jets and two photons. If both photons go undetected or are grouped with the jets, these events can be an irreducible background to the high mass missing energy Higgs search ($e^+e^- \rightarrow hZ \rightarrow b\bar{b}\nu\bar{\nu}$) (as described in section 4.2.2). As such, the double radiative events ($q\bar{q}(\gamma\gamma)$) should be well understood and the Monte Carlo simulations of this process should be in good agreement with the data.

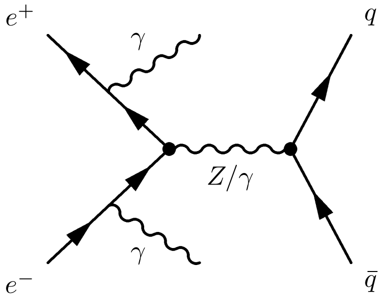

Figure B.1. $e^+e^- \rightarrow q\bar{q}(\gamma\gamma)$.

B.2 Data and Monte Carlo Samples

The data studied was collected by the L3 detector in the year 2000 at center-of-mass energies between 200 GeV and 209 GeV. A total integrated luminosity of 217.8 pb^{-1} was used.

The hadronic signal and background ($e^+e^- \to q\bar{q}(\gamma\gamma)$ and $e^+e^- \to q\bar{q}(\gamma)$, respectively) were simulated with KK2f [11] Monte Carlo. The other Standard Model backgrounds were modelled with PYTHIA ($e^+e^- \to ZZ, Ze^+e^-$), KORALW [12] ($e^+e^- \to W^+W^-$), EXCALIBUR [13] ($e^+e^- \to q\bar{q}'e\nu_e$) and PHOJET [14] ($e^+e^- \to e^+e^-q\bar{q}$).

The L3 detector response is simulated using the GEANT [15] program, which takes into account the effects of multiple scattering, energy loss and showering inside the detector. Time dependent detector inefficiencies, monitored throughout the data taking, are simulated as well. The GHEISHA [16] program is used to simulate hadronic interactions within the detector.

B.2.1 Signal definition

In the double radiative events that are of interest in this study, photons of similar energies are emitted from both incoming positron and electron. The $q\bar{q}(\gamma\gamma)$ signal is defined here by cuts made at the generator level on the kinematic properties expounded below [43]. Assuming that the photons are emitted back-to-back, their energies are related:

$$E_{\gamma 1} = \sqrt{s}/2 - M_Z^2/(2\sqrt{s} - 4E_{\gamma 2}) \tag{B.1}$$

In the case of single radiative return, we set $E_{\gamma 2} = 0$ in equation B.1 above to find,

$$E_\gamma^{single} = (s - M_z^2)/2\sqrt{s} \tag{B.2}$$

To take into account the width of the Z, we set a range of ± 10 GeV ($\pm 4\Gamma_Z$) around the its mass. To avoid the single radiative events, an upper bound is set on the energy of the most energetic photon:

$$E_{\gamma 1} < (s - (M_Z + 10)^2)/2\sqrt{s} \tag{B.3}$$

This maximum photon energy cut will also reject double radiative background events where the second photon comes from final state radiation [44]. The requirement on the energy of the second most energetic photon is found by inserting the maximum energy of the most energetic photon into equation B.1:

$$E_{\gamma 2} > \sqrt{s}/2 - M_Z^2/(2\sqrt{s} - 4E_{\gamma 1}^{max}) \tag{B.4}$$

where $E_{\gamma 1}^{max}$ is the maximum energy of the most energetic photon, as defined by equation B.3.

An additional cut on the angle between the photons is made to ensure that a single radiative event isn't confused with a double radiative event that has its photons close together:

$$\Delta_{\theta_1 \theta_2} = |\theta_1 - \theta_2| > 90^o. \tag{B.5}$$

Events from the $q\bar{q}$ Monte Carlo (KK2F) that do not pass these cuts are considered background.

B.3 Analysis

B.3.1 Preselection

In the preselection, high multiplicity, two-jet events are selected. The same preselection cuts that are described in section 5.1.1 are applied in this analysis. The only exceptions are the exclusion of the cuts on $|\text{cosine}(\theta_{P_{missing}})|$ and the b-tag vari-

Process	Events
$q\bar{q}$(background)	89.0
W^+W^-	193.1
$qq'e\nu_e$	60.1
ZZ	40.6
Ze^+e^-	5.5
$e^+e^-q\bar{q}$	30.6
total background	315.9
$q\bar{q}(\gamma\gamma)$ (signal)	212
total expected	630
data	694

Table B.1. Events left after the $q\bar{q}(\gamma\gamma)$ preselection.

able. With these cuts deactivated, a larger sample of signal ($q\bar{q}(\gamma\gamma)$) events can be examined. Unfortunately, at the same time, releasing these cuts introduces some contamination from two-photon ($e^+e^- \to e^+e^-q\bar{q}$) events. The backgrounds are reduced as described earlier in this work. After preselection, 694 data events are observed while 631±25 events are expected from the Monte Carlo. The breakdown by background type is given in table B.1. The signal efficiency after preselection is 94% and the purity of the sample (S/S+B) is 34%.

B.3.2 Selection

The selection process utilizes an artificial neural network to separate $q\bar{q}(\gamma\gamma)$ signal from the aforementioned backgrounds. The structure of this network is described in section 5.1.3. The six input variables to the network are:

- Maximum jet width
- Acollinearity
- $P_{missing}/P_{total}$
- $P_{missing}/E_{visible}$
- Fitted mass
- $(M_{missing} + M_{visible})/\sqrt{s}$

The distributions for these variables are shown in figure B.2. All of the variables provide good separation of signal and background. The maximum jet width and acollinearity variables (both defined in section 5.1.3) do well separating the signal from W^+W^- background. Both $P_{missing}/P_{total}$ and $(M_{missing}+M_{visible})/\sqrt{s}$ have good discriminating power against W^+W^- and ZZ processes. The fitted mass (described in section 5.1.2) and $P_{missing}/E_{visible}$ variables are best at separating signal from ZZ background.

The distribution of the output of the neural network is shown in figure B.3. As in the ZZ analysis described in the previous appendix, a benchmark cut at 0.5 is made on the neural network output. After this cut, there are 157 events expected and 183 events observed with a signal efficiency of 51%.

B.4 Results

A binned maximum likelihood fit is done to establish the compatibility of data and Monte Carlo. The output of the fit is the ratio of the observed cross section over the expected cross section. The systematic uncertainty is due to the signal and background Monte Carlo statistics, a variation of ± 2% of the energy scale in the calorimeters, the background normalization, and the center-of-mass binning. For this analysis, the ratio of cross sections is

$$R_{\frac{\sigma_{obs}}{\sigma_{exp}}} = 1.23 \pm 0.11 \ \pm 0.10 \tag{B.6}$$

where the first error is statistical and the second is systematic. This measurement is in agreement with the Standard Model expectation.

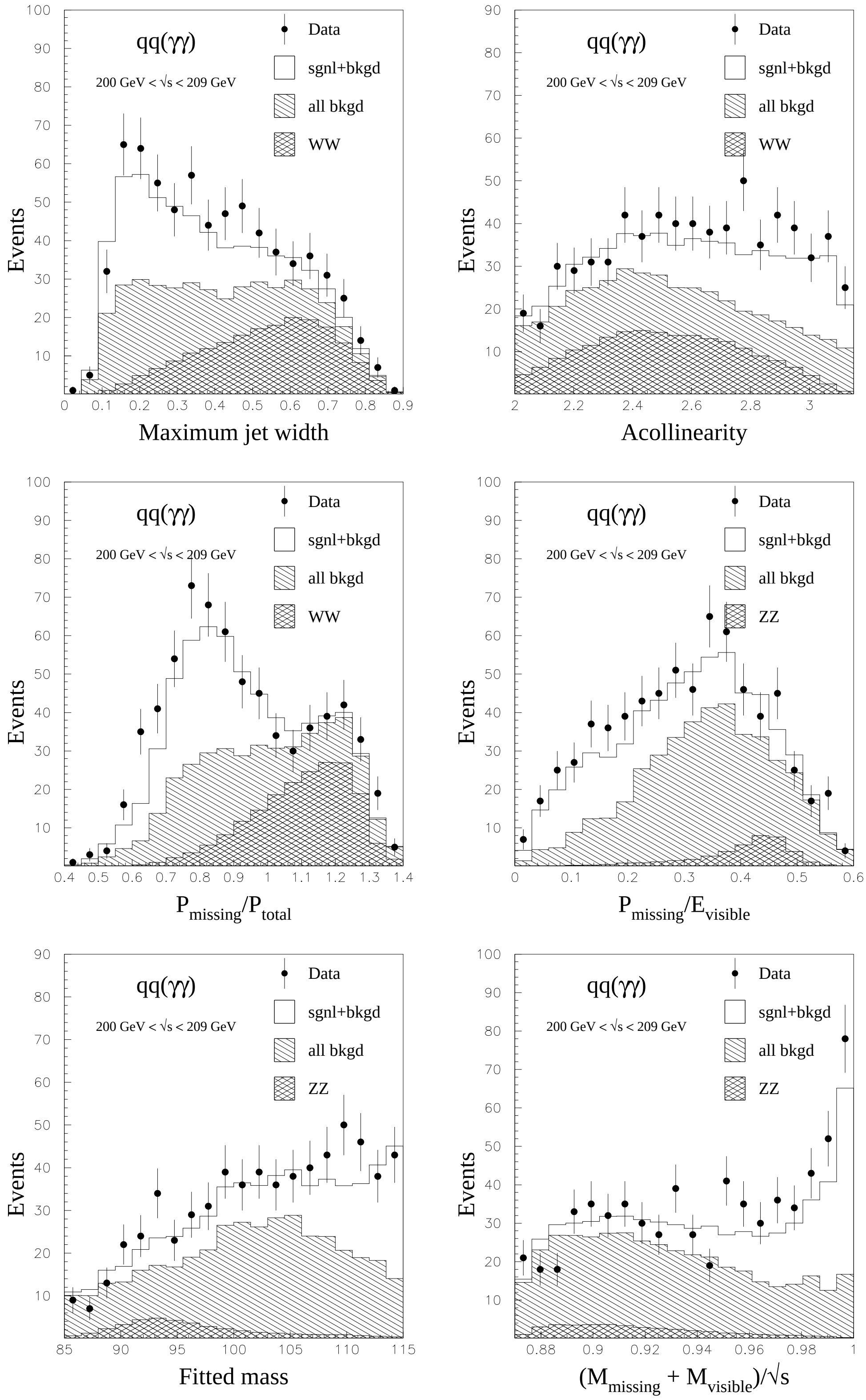

Figure B.2. Input distributions for the $q\bar{q}(\gamma\gamma)$ neural network: maximum jet width, acollinearity, $P_{missing}/P_{total}$, $P_{missing}/E_{visible}$, Fitted mass, $(M_{missing} + M_{visible})/\sqrt{s}$

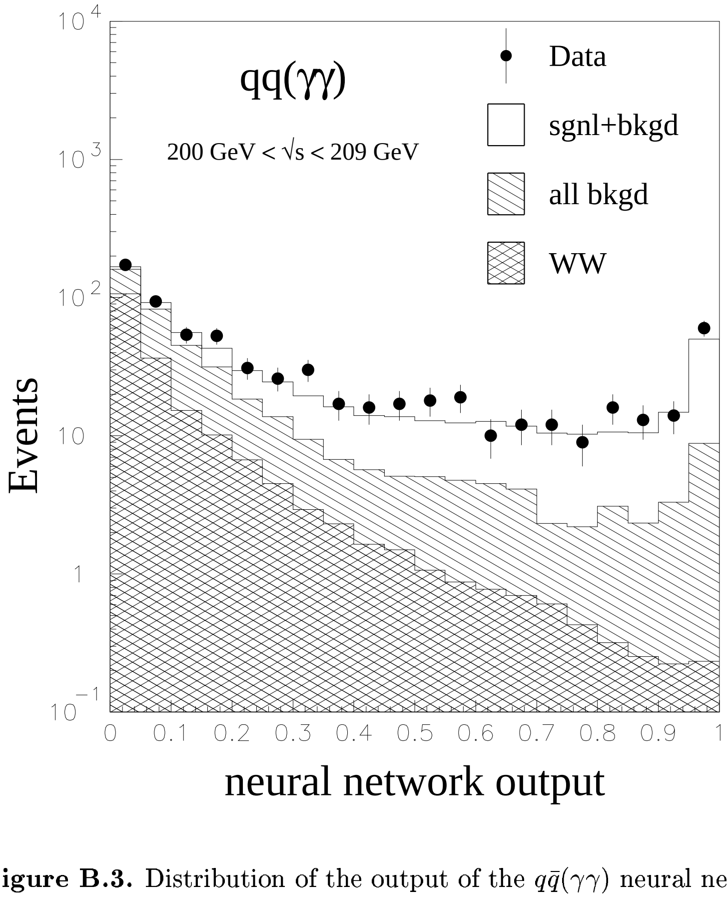

Figure B.3. Distribution of the output of the $q\bar{q}(\gamma\gamma)$ neural network

BIBLIOGRAPHY

BIBLIOGRAPHY

[1] S.L. Glashow, Nucl. Phys. **22** (1961) 579;
S. Weinberg, Phys. Rev. Lett. **19** (1967) 1264;
A. Salam, "Elementary Particle Theory", Ed. N. Svartholm, Stockholm, "Almquist and Wiksell", (1968), 367.

[2] Particle Data Group, D.E. Groom *et al.*, European Physical Journal **C 15** (2000) 1.

[3] The UA1 Collaboration, G. Arnison *et al.*, Phys. Lett. **B 122** (1983) 103.
The UA2 Collaboration, M. Banner *et al.*, Phys. Lett. **B 122** (1983) 476.

[4] The UA1 Collaboration, G. Arnison *et al.*, Phys. Lett. **B 126** (1983) 398.
The UA2 Collaboration, P. Bagnaia *et al.*, Phys. Lett. **B 129** (1983) 130.

[5] P. Janot, "The HZHA generator", in "Physics at LEP2", CERN Report 96-01 (1996).

[6] M. Acciarri *et al.*, Nucl. Inst. Meth. **A 351** (1994) 300.

[7] G. Basti *et al.*, Nucl. Inst. Meth. **A 374** (1996) 293.

[8] I. C. Brock *et al.*, Nucl. Inst. Meth. **A 381** (1996) 236.

[9] The L3 Collaboration, O. Adriani *et al.*, Physics Reports **236** (1993) 1.

[10] PYTHIA versions 5.722 and 6.1 are used.
T. Sjöstrand, Preprint CERN-TH/7112/93 (1993), revised August 1995; Comp. Phys. Comm. **82** (1994) 74; Preprint hep-ph/0001032 (2000).

[11] KK2F version 4.13 is used;
S. Jadach, B. F. L. Ward and Z. Wąs, Comp. Phys. Comm. **130** (2000) 260.

[12] S. Jadach *et al.*, Comp. Phys. Comm. **94** (1996) 216;
S. Jadach *et al.*, Phys. Lett. **B 372** (1996) 289.

[13] F. A. Berends, R. Kleiss and R. Pittau, Nucl. Phys. **B 424** (1994) 308; Nucl. Phys. **B 426** (1994) 344; Nucl. Phys. (Proc. Suppl.) **B 37** (1994) 163; R. Kleiss and R. Pittau, Comp. Phys. Comm. **85** (1995) 447; R. Pittau, Phys. Lett. **B 335** (1994) 490.

[14] PHOJET version 1.05 is used.
R. Engel, Z Phys. **C 66** (1995) 203;
R. Engel and J. Ranft, Phys. Rev. **D 54** (1996)4244.

[15] GEANT version 3.15 is used.
R. Brun *et al.*, Preprint CERN-DD/EE/84-1 (1984), revised 1987.

[16] H. Fesefelt, Preprint PITHA 85/02, RWTH Aachen (1985).

[17] KORALZ version 4.02 is used.
S. Jadach, B. F. L. Ward and Z. Wąs, Comp. Phys. Comm. **79** (1994) 503.

[18] S. Jadach *et al.*, Phys. Lett. **B 390** (1997) 298.

[19] F. A. Berends, P. H. Daverfelt and R. Kleiss, Nucl. Phys. **B 253** (1985) 441;

Comp. Phys. Comm. **40** (1986) 285.

[20] Ian Fisk, "Search for Neutral Higgs Bosons in Electron-Positron Interactions at 189 GeV," Ph.D. Dissertation, UCSD (1999).

[21] S. Likhoded *et al.*, L3 Note 2664, May 14, 2001. [1]

[22] Kirkpatrick, S., Gelatt, C.D. and Vecchi, M.P. (1983). "Optimization by simulated annealing." *Science, 220*, 671-680.

[23] Rumelhart, McClelland, and the PDP Research Group, *Parallel Distributed Processing: Explorations in the Microstructure of Cognition. Volume 1: Foundations*, The MIT Press (1995).

[24] Lönnblad et al., Nucl. Physics **B349** (1991) 675-702.

[25] Byron P. Roe, Probability and Statistics in Experimental Physics, 2nd edition, Springer Verlag (2001).

[26] The L3 Collaboration, M. Acciarri *et al.*, Phys. Lett. **B 495** (2000) 18.

[27] The L3 Collaboration, M. Acciarri *et al.*, Phys. Lett. **B 517** (2001) 319-331.

[28] The LEP working group for Higgs boson searches, "Searches for Higgs bosons: Preliminary combined resultsusing LEP data collected at energies up to 202 GeV", CERN-EP/2000-55, 2000.

[29] The L3 Collaboration, M. Acciarri *et al.*, Phys. Lett. **B 411** (1997) 373.

[30] B. A. Kniehl, Phys. Rep. **C 240** (1994) 211.
E. Gross, B. A. Kniehl and G. Wolf, Z. Phys. **C 63** (1994) 417; erratum-ibid **C 66** (1995) 321.

[31] M. Krämer, W. Kilian, P. M. Zerwas, Phys. Lett. **B 373** (1996) 135.

[32] A. Djouadi *et al.*, Z. Phys. **C 70** (1996) 427.

[33] Marta Felcini, private communications.

[34] R. Berbeco *et al.*, L3 Note 2688, June 25, 2001.[1]

[35] Aleph, Delphi, L3 and Opal Collaborations, The LEP working group for Higgs boson searches, L3 Note 2699, hep-ex/0107029, July 2001.

[36] Chris Tully, *Recent Results of the LEP combined Higgs Results*, talk given at Geneva University, November 2000.

[37] Y. K. Kim, "Tevatron: recent results, present status and future prospects", LP Roma 2001 (http://www.lp01.infn.it/).

[38] D. Cavalli, "Prospects for Electroweak Physics at LHC", EPS Budapest 2001 (http://www.hep2001.elte.hu/).

[39] The L3 Collaboration, L3 Note 2696, July 4, 2001.[1]

[40] The L3 Collaboration, M. Acciarri *et al.*, Phys. Lett. **B 450** (1999) 281-293.

[41] The L3 Collaboration, M. Acciarri *et al.*, Phys. Lett. **B 479** (2000) 101-117.

[42] The L3 Collaboration, M. Acciarri *et al.*, Phys. Lett. **B 497** (2001) 23.

[43] C. Mariotti, E. Piotto, "Symmetric double radiative return events at LEP2", DELPHI 99-155 PHYS 833, October 11, 1999.

[44] The L3 Collaboration, M. Acciari *et al.*, Phys. Lett. **B 505**, (2001), 47-58.

---

[1] L3 notes are freely available upon request from The L3 Secretariat, CERN, CH-1211 Geneva 23, Switzerland. Internet: http://l3www.cern.ch/note/notes.html